



Multi-omic and spatial analysis of mouse kidneys highlights sex-specific differences in gene regulation across the lifespan

Received: 9 October 2022

Siqi Chen^{1,2,12}, Ruiyang Liu^{1,2,12}, Chia-Kuei Mo^{1,2,12}, Michael C. Wendt^{1,2,3}, Andrew Houston^{1,2}, Preet Lal¹, Yanyan Zhao¹, Wagma Caravan^{1,2}, Andrew T. Shinkle¹, Atieh Abedin-Do¹, Nataley Naser Al Deen^{1,2}, Kazuhito Sato^{1,2}, Xiang Li^{1,2}, André Luiz N. Targino da Costa^{1,2}, Yize Li^{1,2}, Alla Karpova^{1,2}, John M. Herndon^{1,4}, Maxim N. Artyomov^{1,5}, Joshua B. Rubin^{6,7}, Sanjay Jain^{1,5,6}, Xue Li⁸, Sheila A. Stewart^{1,9,10}, Li Ding^{1,2,10,11}✉ & Feng Chen^{1,9,10}✉

Accepted: 11 March 2025

Published online: 21 April 2025

Check for updates

There is a sex bias in the incidence and progression of many kidney diseases. To better understand such sexual dimorphism, we integrated data from six platforms, characterizing 76 kidney samples from 68 mice at six developmental and adult time points, creating a molecular atlas of the mouse kidney across the lifespan for both sexes. We show that proximal tubules have the most sex-biased differentially expressed genes emerging after 3 weeks of age and are associated with hormonal regulations. We reveal potential mechanisms involving both direct and indirect regulation by androgens and estrogens. Spatial profiling identifies distinct sex-biased spatial patterns in the cortex and outer stripe of the outer medulla. Additionally, older mice exhibit more aging-related gene alterations in loops of Henle, proximal tubules and collecting ducts in a sex-dependent manner. Our results enhance the understanding of spatially resolved gene expression and hormone regulation underlying kidney sexual dimorphism across the lifespan.

The kidney has fundamental roles in fluid homeostasis, blood filtering, reabsorbing important molecules¹ and processing hormones that regulate blood pressure and bone mineralization². An aspect of substantial biomedical interest is sex differences manifested in gene expression^{2–11}, as incidence and severity of injury^{12,13} and higher risk for males of kidney cancer¹⁴ due to presumed hormonal protective effects in females^{8,15}. Other factors, like age, lifestyle and sex chromosomes, also contribute to this dimorphism¹⁶. While these differences have been investigated with respect to structure, physiology, pathologies and pharmacological responses, the underlying molecular mechanisms regulating the spatial transcriptional dimorphism, especially across the lifespan, are less understood.

Recent advances in single-cell technologies now enable deeper molecular insights^{2,17–25} and, when combined with bulk RNA and assay for transposase-accessible chromatin with sequencing (ATAC-seq) in mouse studies, have identified distinct expression profiles in proximal nephron segments between sexes at individual time points^{2,4}. However, variations in spatial gene expression and regulatory networks between sexes remain unclear. As part of the GenitoUrinary Development Molecular Anatomy Project and Cellular Senescence Network consortia, we investigated kidney developmental and aging differences between male and female mice through the integration of six technologies, namely single-nucleus RNA sequencing (snRNA-seq), single-nucleus ATAC-seq (snATAC-seq), Visium spatial transcriptomics (ST), Xenium

ST, multiplexed imaging and immunofluorescence (IF). Data were generated at six time points across the lifespan, from embryonic day 16.5 (E16.5), newborn (P0), adolescent (3 weeks), adult (12 and 52 weeks), to old age (92 weeks) of both sexes. We discovered 385 sex-biased genes in the proximal tubule (PT), examined hormone regulation differences and revealed insights into kidney sexual dimorphic regulation over the organismal lifespan.

Results

Integrated multi-omics analyses of the mouse kidneys

We collected kidneys from C57BL/6J mice of both sexes at E16.5, P0, week 3 (W3), week 12 (W12), week 52 (W52) and week 92 (W92). These time points correspond approximately to the embryo, newborn, youth, adolescence, adult and old age in humans (Supplementary Table 1). From snRNA-seq and snATAC-seq, we recovered 203,139 high-quality cells across all samples. Quality control metrics indicated no systematic bias among biological replicates (Supplementary Fig. 1a–c and Source Data Fig. 1). All samples showed the expected insert size with a strong enrichment of signal at transcription start sites, indicating high snATAC-seq data quality (Supplementary Fig. 2), with 76.9% of the peaks also shown in a recently published mouse kidney single-cell ATAC-seq dataset¹⁷. Samples from different ages and sexes also exhibited good expression-based correlation across cell types before and after Soupx-based ambient RNA removal (Supplementary Fig. 3), indicating ambient RNA is not an important confounder. To control for any potential batch effect, we performed downstream analysis with Harmony-based²⁶ batch-corrected data (Methods).

Our initial multi-omic dataset consisted of snRNA-seq, snATAC-seq and Visium ST for normal kidneys spanning the whole lifespan (Fig. 1a). Cell-type-specific marker expression and top differentially expressed genes (DEGs) for each cell type are shown in Extended Data Fig. 1 and Source Data Extended Data Fig. 1. We applied the robust cell type decomposition (RCTD)²⁷ and CytoSpace²⁸ to resolve the cell types in Visium ST data. As expected, the population structures of E16.5 and P0 shown on Uniform Manifold Approximation and Projection (UMAP) and Visium ST were distinct from later time points (Fig. 1a and Extended Data Fig. 2), especially for progenitor and transitional cells. When comparing UMAPs among ages, sex differences in the PT were noticed starting from W12, while other major populations remain similar between sexes throughout life. While nephron progenitor (NP) cells and fibroblasts formed prominent clusters at E16.5 and P0, tubular epithelial cells expressing segmental specific markers constituted the majority in later time points. The midsagittal section in Visium ST covering all major kidney regions allowed visualization of the full spectrum of cell types with their designated anatomic location. A clear change of cell-type distribution patterns is detected between P0 and W3, reflecting the dramatic development and maturation of kidney cell types during that period (Fig. 1a). Next, we checked known kidney segmental markers²⁹ on Visium ST (Fig. 1b), and those markers correctly outlined the spatial distribution of respective kidney segments. For example, *Slc5a12* (a PT marker) appeared prominently in the cortex region, while *Aqp2* (a collecting duct principal cell (CD_PC) marker) was more apparent in the medulla region. Moreover, using snATAC-seq, we observed tight regulation of each marker by distinctive chromatin accessibility peaks in the cell type defined by a given marker, such as *Slc5a12* for PT segment 1 (PT(S1)), *Slc13a3* for PT segment 2 (PT(S2)) and *Slc7a12* for PT segment 3 (PT(S3))²⁹ (Fig. 1c).

Sex dimorphism in transcription emerges in PT since puberty

To reveal sex differences in different kidney segments along the mouse lifespan, we next analyzed sex-biased DEGs beginning with kidney progenitor populations. We started by examining the gene expression profiles of NP cells and ureteric bud progenitor (UBP) cells because they give rise to all epithelial cells in the kidney and have distinct developmental trajectories.

Among all the cell types, PT cells exhibited the most unique patterns in terms of development and sex difference (Fig. 2a,b and Extended Data Fig. 3). Adjacent PT segments have a group of shared genes while also having unique marker genes. For example, *Slc34a1* is shared between S1 and S2, whereas *Slc5a12* is exclusively expressed in S1. Overall, the W3 kidney has a different gene expression profile compared to later ages, with a small number of genes showing a weak sex bias in expression (Fig. 2a and Extended Data Fig. 3). Interestingly, the expressions of genes such as *Rhobtb1* and *Ehhad* were strongly upregulated at W3 but decreased at later ages in both sexes. On the contrary, the expression of genes such as *Ghr* was absent at W3 but was maintained at high levels in later ages in both sexes. Furthermore, the expressions of genes such as *Slc7a12* and *Napsa* were high at W3, remained at elevated levels for females at later ages, but declined at all later stages in males; transcripts of *Slc7a13*, *Cyp2j13*, *Cyp4b1* and *Slc22a30* were not detected in females throughout the lifespan but were robustly present in males since W12. These genes all exhibited dramatic changes in gene expression patterns between W3 and W12, a period when sexual maturity happens and sex hormone regulation might have an important role in gene expression. Moreover, a group of genes is strongly expressed in males, such as *Cyp2j13* and *Cyp4b1* in PT(S2) and *Atp11a* and *Slc7a13* in PT(S3). On the other hand, a group of genes is exclusively expressed in females, including *Kynu* in PT(S2) and *Slc7a12* in PT(S3). In addition to PT, we also noticed age-dependent expression patterns for the loop of Henle (LOH) ascending limb, distal convoluted tubule (DCT) and collecting duct (CD; Fig. 2a,b and Extended Data Fig. 4), emphasizing the importance of defining cell-type-specific markers for the early developmental stages.

Collectively, we summarized the developing trajectories for NP, UBP and their descendant cells with enriched genes in corresponding periods in Fig. 2c. Sex differences were most abundant in PTs in the mouse kidney, which became apparent between W3 and W12, and such differences are more obvious in the PT(S2) and PT(S3) segments compared to PT(S1).

Sex-biased DEGs are present most frequently in PT(S3)

To systematically examine sex differences across cell types and ages, we performed correlation analyses for each epithelial cell type, using snRNA-seq expression (Extended Data Fig. 5a) and snATAC-seq peak accessibility (Extended Data Fig. 5b). Both heatmaps show clustering by cell type, except for PT segments—S1 and S2 cluster together, while S3 forms a distinct group.

Using snRNA-seq, we identified 353 male-biased and 406 female-biased genes across the three PT segments (Fig. 3a and Supplementary Table 2a,b). Most sex-biased DEGs were found in S3, followed by S2, with very few in S1. Pathway analysis using the Hallmark gene set from MSigDB³⁰ of S3 DEGs (Fig. 3b) revealed female enrichment in myogenesis, interleukin 2 (IL-2)-Signal Transducer and Activator of Transcription 5 (STAT5) signaling and epithelial–mesenchymal transition, while males showed enrichment in xenobiotic and fatty acid metabolism pathways³¹. These findings emphasize the complexity of sex-specific gene regulation in renal physiology and highlight the importance of considering sex as a biological variable in kidney studies.

Correlation analysis of the top 100 DEGs from adult mice showed stronger S2/S3 correlation in males than females (Fig. 3c; blue and red boxes, group 2 versus group 3), consistent with published data from ref. 4 (Extended Data Fig. 6a). S3 also displayed slightly greater sex differences than S2 (Fig. 3c; green and gray boxes, group 1 versus group 4), as highlighted by UMAP clustering (Fig. 3d). Comparing DEGs in PT(S2) and PT(S3) using a published dataset² (Fig. 3e and Source Data Fig. 3; Methods), we confirmed that most sex-biased genes emerged between W3 and W12 in Visium ST (Extended Data Fig. 6b), coinciding with rising sex hormone levels during this period. Specifically, testosterone begins to elevate around P30, estradiol increases between P26 and P29 and progesterone starts as early as P10, with a

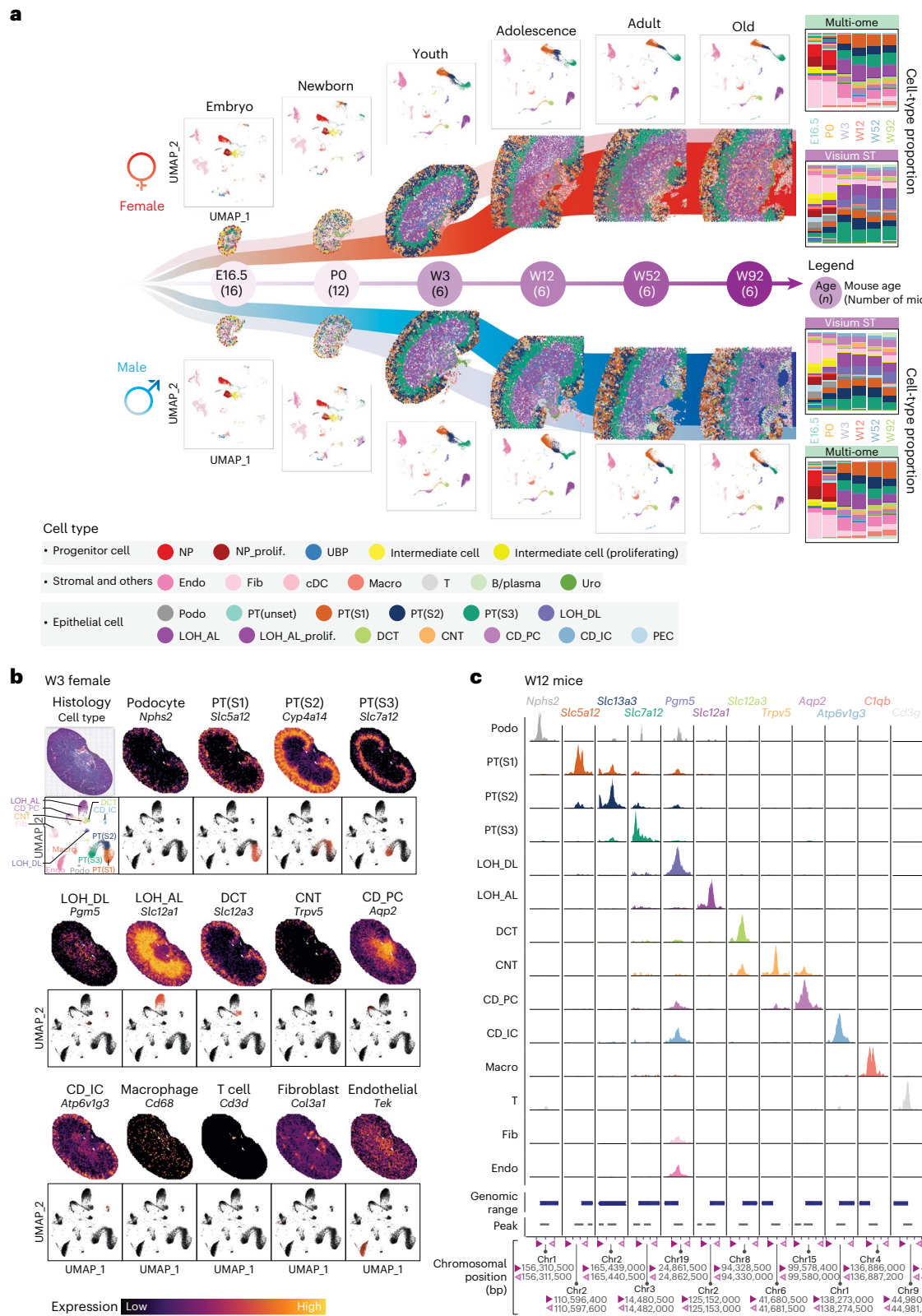


Fig. 1 | Study design and integrated cell-type distribution from Visium ST, snRNA-seq and snATAC-seq. **a**, The study design and multi-omic dataset. Time points and the number of mouse kidneys collected for each time point are shown along the central line. UMAPs from multi-ome and ST images from Visium display cell-type distributions across time points. Bar charts on the right show cell-type proportions. Colors represent different cell types in the legend. **b**, Single nuclei and spatial expression profiles of cell-type marker genes in a W3 female mouse kidney, with expression levels color-coded from low (dark purple) to high

(yellow). **c**, snATAC-seq peak accessibility of major kidney cell types in W12 mice. Cell types are indicated by marker genes, with colors representing accessibility levels. Endo, endothelial cell; Fib, fibroblast; cDC, conventional dendritic cell; Macro, macrophage; Uro, urothelium; Podo, podocyte; LOH_AL, loop of Henle ascending limb; LOH_DL, loop of Henle descending limb; CNT, connecting tubule; CD_IC, collecting duct intercalated cell; PEC, parietal epithelial cells; chr, chromosome; prolif., proliferating.

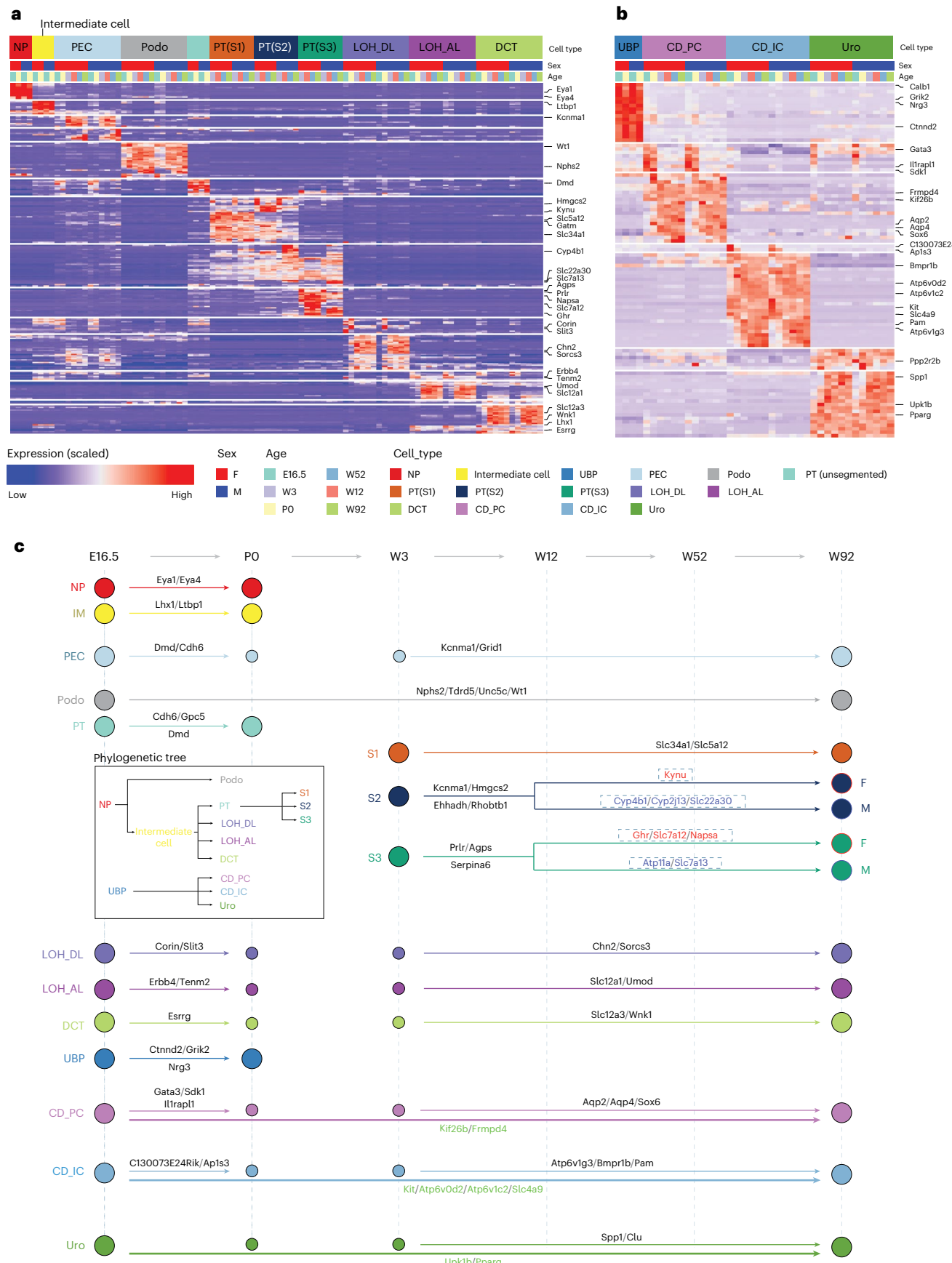


Fig. 2 | Developmental trajectories of main kidney progenitor cells across the lifespan. **a,b,** Heatmaps of the top DEGs for each cell type derived from **(a)** NP cells and **(b)** UBP cells. Each heatmap shows cell types, sex and age in the top three rows. **c,** Developmental trajectories illustrate gene enrichment over time for cells descending from NP and UBP. F, female; M, male.

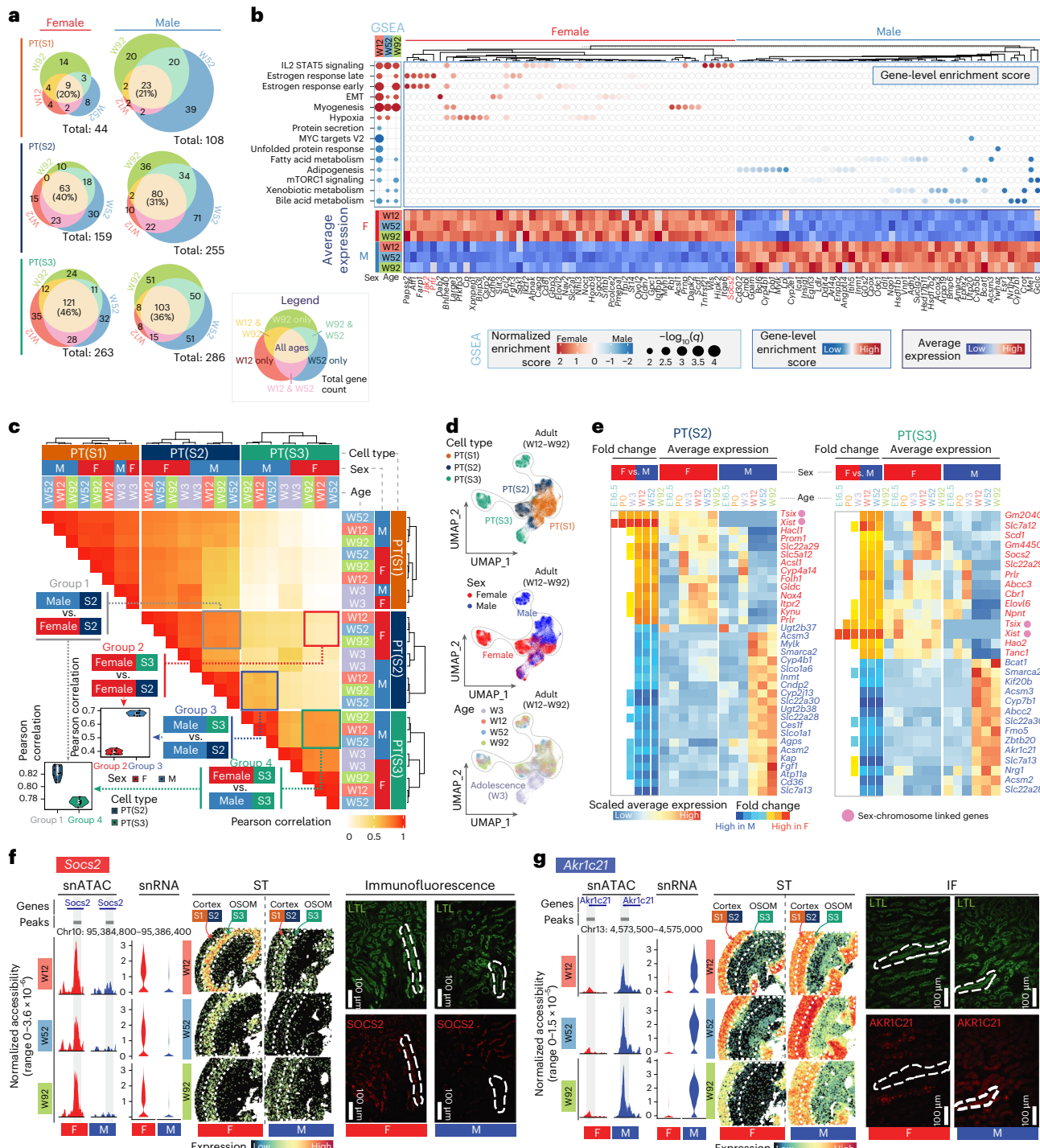


Fig. 3 | Sex-biased DEGs in PT segments. **a**, Euler diagrams for sex-biased DEG counts in each PT segment at adult time points W12, W52 and W92. Numbers represent gene counts for each time point and overlapped time points. Colors representing different time points are indicated in the legend. **b**, Bubble plots for sex-biased normalized enrichment scores (NES) from GSEA (left) and key pathway-related genes weighted by expression levels as gene-level enrichment score (GES) (right). The bottom plot presents the pseudobulk expression of selected genes. **c**, Pairwise Pearson correlation analysis for PT segments and sexes. Red box shows the correlation between PT(S2) and PT(S3) in females, blue box shows the correlation between PT(S2) and PT(S3) in males, green box shows PT(S3) correlation between sexes and gray box shows PT(S2) correlation between sexes. Violin plots on the bottom left show correlation comparisons. **d**, UMAPs show transitions of PT(S1), PT(S2) and PT(S3) from W3 to W92, with dotted lines marking cells from adult kidneys (W12–W92). **e**, Heatmaps for snRNA-based expression of top sex-biased DEGs in PT(S2) and PT(S3). The first group of

columns indicates gene expression FC (orange for female-biased and blue for male-biased), and the next two groups of columns show average expression levels in females and males. **f**, Comparison of *Socs2* expression patterns between sexes via snATAC-seq, snRNA-seq, ST and IF staining. LTL stains identify PT segments; white-dotted curves in ST images mark inner cortical and outer medullary regions, while white-dashed curves in IF staining images highlight PT(S3)-like straight tubules and representative protein expression differences between sexes ($n = 3$). Experiments are repeated >3 times with similar results. Scale bar = 100 μm . **g**, Comparison of *Akr1c21* expression patterns between sexes using snATAC-seq, snRNA-seq, Visium ST and IF staining, with labeling consistent with **f** ($n = 3$). Experiments are repeated more than thrice with similar results. Scale bar = 100 μm . EMT, epithelial-mesenchymal transition; mTORC1, mammalian target of rapamycin complex 1; MYC, MYC proto-oncogene, BHLH transcription factor; LTL, lotus tetragonolobus lectin.

noteworthy increase around P21 (ref. 32). This timing suggests that sex hormones likely drive sexually dimorphic differentiation, reflecting the ‘organizational effects’ of sex steroids in shaping organ development and maturation³³.

Several known sex-biased genes (*Abcc3*, *AcsM2*, *Cyp7b1* and *Prlr*) were validated in our analysis^{2,34–36}. Notably, *Abcc3* and *Prlr* only exhibited sex-biased expression after puberty—their expression levels were similar in both sexes at W3 (Fig. 3e) but rapidly declined in males, while remaining stable in adult females, highlighting a previously overlooked change in gene expression dynamics between sexes when only focused on adult age ranges. We also identified sex-biased genes in PT (Fig. 3e) that have not been previously highlighted²—*Socs2* and *Akr1c21* (Fig. 3f,g and Extended Data Fig. 7a,b). *Socs2* was consistently female-biased in gene expression and chromatin accessibility across ages, particularly in the inner cortex and outer medulla as indicated by Visium, where PT(S3) segments are mainly located. Similarly, *Akr1c21* displayed a consistent male-biased expression and chromatin accessibility trend in PT(S3), but no sex difference in the cortex. Both markers were verified at the protein level, where the lotus tetragonolobus lectin (LTL)-positive long straight tubules highlighted by the dotted lines morphologically resemble PT(S3) (Fig. 3f,g and Extended Data Fig. 7a,b). Both genes are linked to steroid hormone signaling^{37,38}, reinforcing the role of hormonal regulation in kidney sexual dimorphism.

Molecular mechanisms of sex dimorphisms in mouse PT

Next, we examined transcription factor (TF) regulon activities to identify the upstream regulators of sex-biased DEGs (Methods). PT(S1) and PT(S2) share a group of regulons distinct from PT(S3). Most of the regulons enriched in PT(S3) were sex-biased, while regulons in PT(S1) and PT(S2) were not (Fig. 4a and Source Data Fig. 4). The regulon activity-based t-distributed Stochastic Neighbor Embedding (tSNE) plot shows PT(S3) cells were further apart from the partially mixed PT(S1)/PT(S2) population and were separated by sex beginning from W12, aligning with previous DEG patterns (Extended Data Fig. 8a). Notably, regulon enrichment changed markedly between W3 and W12, suggesting sex hormone involvement. Interestingly, we did not observe enrichment of sex hormone-related regulons, consistent with a recent study that had not observed the over-representation of hormone response elements in the promoter region of sex-biased DEGs in mouse kidneys⁴.

We then investigate connections between the sex-biased TFs and DEGs (Extended Data Fig. 8b,c and Fig. 3e). Several female-biased TFs, including *Cebpd*, *Creb3l1* and *Foxql*, may regulate female-biased DEGs *Socs2* and *Jak2*. As *Jak2*/STAT5 signaling regulates *Socs2* and is activated by prolactin^{39,40} and *Prlr* has been reported in ref. 2 as a female-biased DEG, we hypothesized a prolactin-driven female-biased regulatory network in PT(S3) through the PRLR/JAK/STAT signaling pathway. In this model, prolactin binds PRLR, activating JAK2/STAT5 to upregulate *Socs2* (Fig. 4b).

Additionally, the male-biased TF BCL6 represses *Socs2* expression⁴¹, sharing a mutually exclusive promoter binding site with STAT5 between sexes⁴². In females, STAT5 likely binds and activates *Socs2*, while in males, BCL6 binds and represses it. Interestingly, from all female-biased genes of PT(S3), only *Socs2* and *Prlr* promoters contain STAT5 and BCL6 binding motifs, suggesting a unique competitive binding mechanism (Fig. 4c and Extended Data Fig. 9a,b) of STAT5/BCL6 on the PRLR/SOCS2 pathway. Other female-biased DEGs, such as *Abcc3* and *Acot7*, are the downstream targets of STAT5, but not BCL6 (Fig. 4d), and appear to be regulated solely by the prolactin-induced JAK2/STAT5 activation without the involvement of BCL6.

In summary, we propose the following two mechanisms regulating female-biased DEGs in PT(S3): prolactin-induced JAK2/STAT5 activation and STAT5/BCL6 competitive binding at target promoters. *Socs2* and *Prlr* expressions are likely controlled by both mechanisms, while *Abcc3* and *Acot7* rely on JAK2/STAT5 alone (Fig. 4e). Because prolactin

is estrogen-regulated^{43,44}, this pathway exemplifies potential indirect estrogen control over female-biased DEGs. The STAT5/BCL6 competitive regulation on *Socs2* and *Prlr* is intriguing as this mechanism is known for liver sex dimorphisms^{42,45} and pulmonary hypertension^{46,47}. Our study now links STAT5/BCL6 competitive binding to sex dimorphisms in kidneys, highlighting the complex interplay of activators and repressors driving sex-biased gene regulation—while the sex difference of *Socs2* chromatin accessibility was not as obvious as other sex-biased DEGs (Fig. 3f and Extended Data Fig. 9a), the involvement of both activators and repressors between sexes likely contributes more to sex-biased genes like *Socs2*.

Sex-biased spatial distribution patterns

Using the single-cell spatial platform Xenium, we analyzed spatial expression patterns for kidneys from female and male mice at W12 and W92 (Supplementary Table 3; Methods). Based on histology and cell-type compositions, we identified the following four distinct kidney zones: cortex, outer stripe of the outer medulla (OSOM), inner stripe of the outer medulla and inner medulla (IM; Fig. 5a,b). Female kidneys had a thinner cortex and thicker outer medulla than males.

We identified five distinct sexually dimorphic spatial expression patterns based on expression characteristics of cortex and OSOM (Fig. 5c,d and Extended Data Fig. 9c). Pattern 1 was highly expressed in male cortex and OSOM, pattern 2 was highly expressed in male OSOM, pattern 3 was highly expressed in male cortex, pattern 4 was highly expressed in male cortex and female OSOM and pattern 5 was highly expressed in female OSOM. Patterns 1, 3 and 5 displayed higher gene expression levels either in males or females, while patterns 2 and 4 demonstrated more complex dynamics (Fig. 5c,d)—pattern 2 showed cortex expression in both sexes but higher expression in male OSOM; pattern 4 highlights a sex-biased DEG that can be male-biased and female-biased simultaneously in different kidney zones. This demonstrated the importance of studying sex dimorphism in kidneys with the spatial content.

Next, we quantified the spatial expression of key genes *Pigr* (pattern 1) and *Akr1c21* (pattern 2) along the proximal-to-distal axis of the kidney zones (Fig. 5e–h), using segmental markers *Lrp2* and *Aqp7* to define PT and PT(S3), respectively. *Pigr*, a pattern 1 gene, peaks at the corticomedullary junction within PT(S3), revealing a previously unrecognized polarized spatial expression (Fig. 5e,f). Similarly, *Akr1c21* exhibits a male-specific enrichment in PT(S3) and a sharp expression drop in female OSOM (Fig. 5g,h), consistent across platforms, with male-biased expression in PT(S3) of OSOM (Fig. 3g).

We also examined female-biased genes (*Prlr*, *Jak2* and *Socs2*) from pattern 5 (Fig. 5i–k and Extended Data Fig. 9d), involved in the JAK/STAT pathway identified through snRNA-seq and snATAC-seq (Fig. 4d). These genes show higher expression in female PT(S3), with trend plots highlighting a sharp expression peak in the OSOM (Fig. 5k). This hinted at a unique female-biased hormonal regulation in OSOM.

Nuclear receptors (NRs) regulate sex-biased DEGs in PT

To investigate chromatin regions controlling sex differences in mouse kidneys, we performed motif enrichment analysis to identify sex-enriched motifs from differentially accessible chromatin regions (DARs; Source Data Fig. 6; Methods). Focusing on PT(S2) and PT(S3), we identified sex-specific motifs (Fig. 6a,b). For example, the C/EBP family is highly enriched in females, whereas NR1, NR2 and NR3 are enriched in males. The POU domain factors exhibit more complicated patterns. In S2, POU4/POU6 are enriched in males, while in S3, POU1/POU2/POU3/POU5 are more enriched in females.

Steroid receptors belong to the NR family⁴⁸. Because we are particularly interested in sex hormone regulations in kidneys, we next performed a systematic analysis for all NR family motifs. As indicated in orange in Fig. 6c, sex-biased motifs (Methods) were mostly found within the NR1/NR2/NR3 subgroups in PT(S2) and PT(S3). Furthermore,

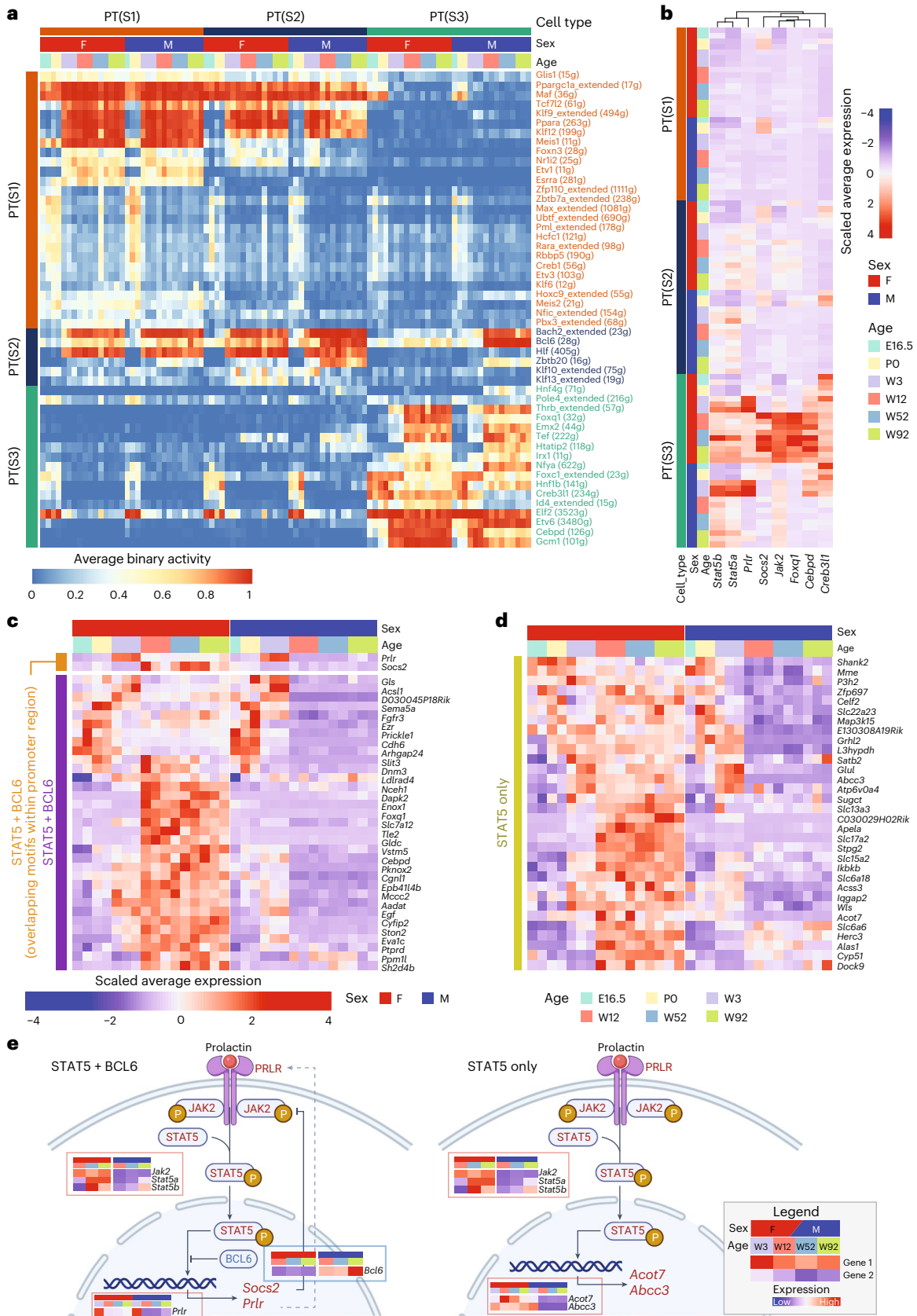


Fig. 4 | Sex differences in PT revealed by regulatory network analysis. **a**, Heatmap for the averaged binary activity of cell-type-specific regulons in PT segments across all samples from age E16.5 to W92. Top rows indicate cell type, sex and age. The '(number g)' notation indicates the number of genes in the regulon. **b**, Heatmap of genes involved in *Socs2* expression regulation. **c**, Expression of PT(S3)-derived, female-biased genes predicted to be

downstream targets of both STAT5 and BCL6 (**c**) and controlled strictly by STAT5 (**d**). Reference bars on top indicate sex and age. **e**, Sex-biased regulatory mechanism diagram, controlled by STAT5 and BCL6 together (left), or controlled by STAT5 alone (right). Red boxes show female-biased genes and blue boxes show male-biased genes.

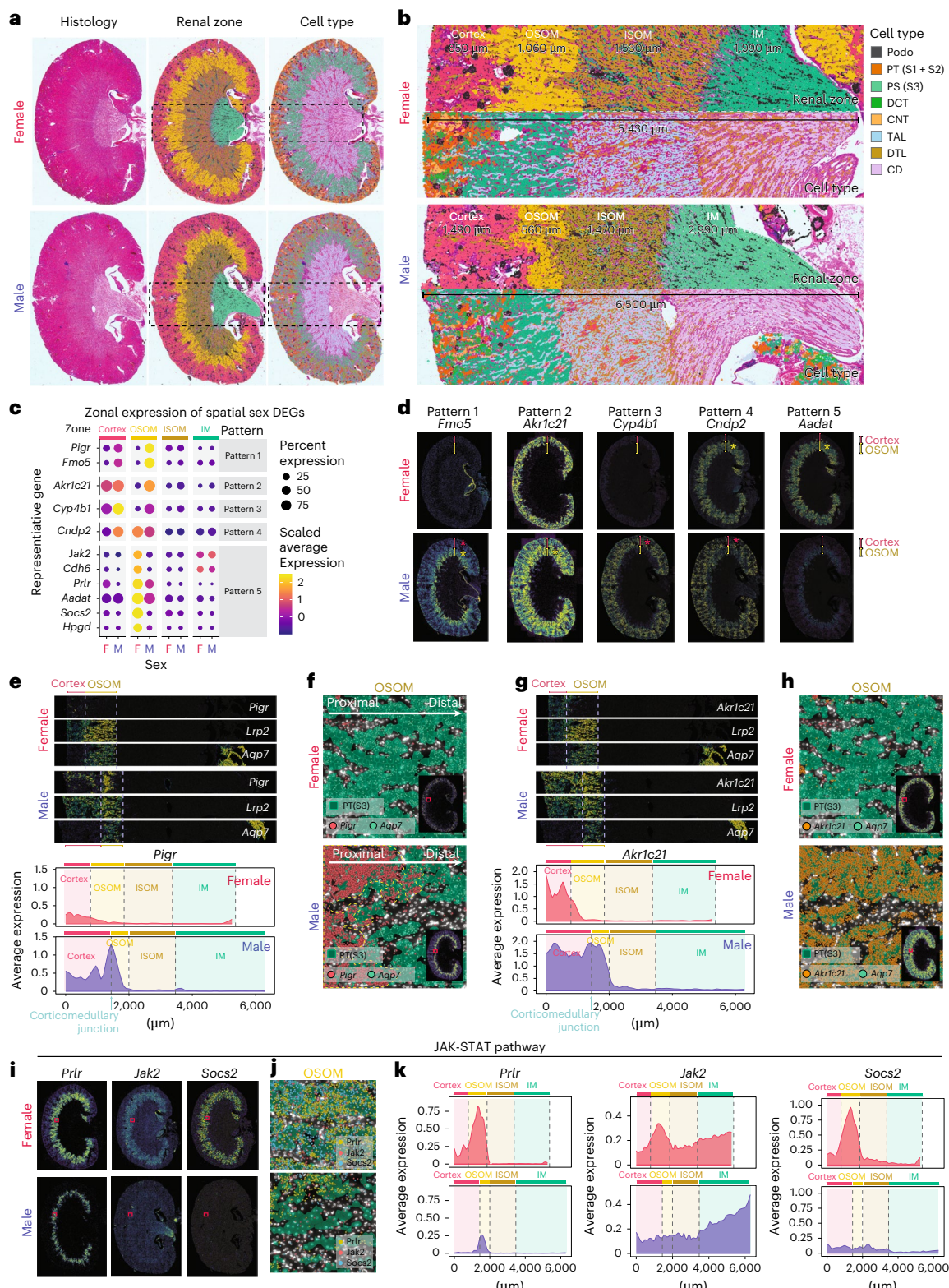


Fig. 5 | Sex-biased spatial distribution patterns revealed by Xenium. a, H&E images, spatially resolved renal zones and cell types of W92 kidneys generated by Xenium for demonstration ($n = 1$ for each sex). Dashed boxes indicate zoomed regions in the next panel. **b**, Magnified view of renal zones and tubular cell types in female and male kidneys. **c**, Bubble plot of average and percent expression levels for each pattern. **d**, Single-cell sex-biased spatial expression patterns. **e**, Top, cropped spatial expression pattern of male-biased gene *Pigr*, along with PT and PT(S3) markers *Lrp2* and *Aqp7*, respectively. Bottom, average expression trend plot of *Pigr* in the cropped region (Method). **f**, Zoomed OSOM view of *Pigr*, *Aqp7* and PT(S3) in female and male mouse kidneys. **g**, Top, cropped spatial

expression pattern of male-biased gene *Akr1c21*, along with PT and PT(S3) markers *Lrp2* and *Aqp7*, respectively. Bottom, average expression trend plot of *Akr1c21* in the cropped region. **h**, Zoomed OSOM view of *Akr1c21*, *Aqp7* and PT(S3) in female and male mouse kidneys. **i**, Single-cell spatial expression profile of *Prlr*, *Jak2* and *Socs2* in kidneys of both sexes. **j**, Zoomed-in view of *Prlr*, *Jak2*, *Socs2* and PT(S3) in the OSOM zone mouse kidneys of both sexes. **k**, Expression trend plot of *Prlr*, *Jak2* and *Socs2* in the cropped region. ISOM, inner stripe of the outer medulla; TAL, loop of Henle thick ascending limb; DTL, loop of Henle thin descending limb.

all enriched motifs are only enriched in males. Meanwhile, none of the estrogen-related motifs (ESR1, ESR2, ESRRA, ESRRB and ESRRG) exhibited an enrichment pattern in either sex (Fig. 6d), which aligns with the report from ref. 4 indicating the female-biased DEGs are not directly regulated by estrogen. In contrast, the androgen receptor (AR) motif showed a significantly higher enrichment in males in all three PT segments, suggesting a direct involvement of androgen in sex-biased motif enrichment in the male kidney. Compared to the NR3 subgroup, NR1 and NR2 are highly enriched in male PT(S3), especially HNF4A (var.2), HNF4G and HNF4A. This suggests that NR1 and NR2 shape both the male PT segment differences and the sex dimorphism, while NR3s only drive sex differences. Among all the male-biased DEGs in three PT segments, we found that around 14% are the downstream targets of the AR motif (Fig. 6e), including well-known ones such as *Slco3a1*, *Serpinf2*, *Slc7a13*, *Slc22a30*, *Cyp4b1* and *Acsm2*.

Evaluate mouse PT sex DEGs in human

We next evaluated our mouse-based discovery in human samples²⁵ (Supplementary Table 4). Major tubular epithelial cell populations were identified in the single-cell dataset²⁵ (Extended Data Fig. 10a). Consistent with the mouse results, PT was the cell type having the largest number of sex DEGs in humans (Extended Data Fig. 10b). We found that 87% (906) and 82% (796) sex DEGs showed the same trend in both species for females and males, respectively. There were 135 and 111 overlapping DEGs showing greater than twofold expression differences in both mice and humans (Fig. 7a). For example, *SPP1* had a higher expression in females, a finding validated by Visium ST (Fig. 7b). Upregulation of *SPP1* has been observed in multiple kidney diseases, including acute kidney injury (AKI) and chronic kidney disease (CKD)⁴⁹. Among genes with sex differences in PT (Source Data Fig. 3), the male-biased DEG *Dock5* was expressed at a higher level in clear cell renal cell carcinomas (ccRCC) compared to normal adjacent tissue. Higher expression of *Dock5* was associated with worse survival in male patients with ccRCC ($P = 0.022$, hazard ratio (HR) = 1.5, 95% confidence interval (CI) = 1.1–2.1), but not in female patients with ccRCC ($P = 0.231$, HR = 0.75, 95% CI = 0.47–1.2; Fig. 7c). The oncogenic role of *Dock5* has been reported in head and neck squamous cell carcinoma⁵⁰ and lung adenocarcinoma⁵¹ to promote invasion and metastasis⁵², while it is unclear if it has similar functions in ccRCC.

We further investigated human/mouse consistency at the protein level using IF staining and multiplexed imaging (PhenoCycler). SOCS2, SCD, CYP4B1 and indolethylamine N-methyltransferase (INMT) showed significant sex differences in human kidney PT cells, verified in three independent pairs (Fig. 7d–g, Supplementary Figs. 4–7 and Supplementary Table 4). Consistently, SOCS2 and SCD showed significantly higher expression in female PT cells, while CYP4B1 and INMT were higher in male PT cells. *Cyp4b1* also exhibits a sex-biased spatial expression pattern in the male mouse cortex in Xenium (Fig. 5c,d). Using multiplexed imaging with a panel of 22 markers (Supplementary Table 5 and Fig. 7h–j), we identified higher SOCS2 expression in tubules in the female mice kidneys. The differences observed in the thick ascending limb of the LOH, DCT or CD were not statistically significant (Fig. 7k). This indicates that SOCS2 has a higher protein expression level in female human PTs, but not in other nephron segments.

Aging affects different cell types between sexes in the kidneys

To investigate sex differences in aging kidneys, we compared W92 kidneys to younger ages (Fig. 8a). After reclustering, we found immune cells, namely macrophages (C9), dendritic cells (C22), T cells (C17) and B/plasma cells (C20 and C28), showed steadily increasing cell proportions from W12 to W92 (Fig. 8b), indicating an accumulation of immune cells in kidneys upon aging.

When comparing the number of age-related DEGs between W12 and W92 kidneys in different cell types (Fig. 8c and Source Data Fig. 8), PT exhibited the largest number of alterations upon aging, and these

differences were much more dramatic in aged males compared to females. On the other hand, CD_PC showed more abundant age-related alterations in females. Next, we explored the DEGs upon aging in PT(S2), PT(S3) and fibroblasts as representatives for epithelial cells and stroma cells because they showed more abundant aging-related DEGs. We found that several aging-related DEGs are also members of SASP and/or on the SenMayo list^{53,54}, such as *Fgf1*, *Pappa* and *Spp1* in PT(S2), and *Serpine2* in PT(S3), indicating that they may have important roles related to senescence in kidney aging (Fig. 8d–f and Source Data Fig. 8).

Some aging-related genes have been reported to be associated with kidney or kidney diseases. For example, we found that *Pappa* was expressed at a much higher level in females, and the expression increased steadily with age (Fig. 8e, red star). Mice without this gene have a 22–43% increase in mean lifespan, and this effect was highlighted most prominently in the kidney among 21 organs⁵⁵, suggesting a potential sex-biased role of *Pappa* in kidneys related to aging. *Spp1*, validated in human samples in the previous section (Fig. 7b), also has increased expression in aging females (Fig. 8e, red star), and it is known to be involved in kidney stone formation^{56,57}. The risk of developing kidney stone diseases increases with age⁵⁸, suggesting a potential contributing role of *Spp1* in kidney stone formation in older females.

Finally, we have noticed that a group of aging DEGs are also the top sex DEGs in our study, such as *Atp11a* and *Smarca2* in S2 and *Acsm3*, *Cyp7b1*, *Hao2* and *Prlr* in S3 (Figs. 3e and 8d,e). As representative male-biased DEGs, *Acsm3* and *Cyp7b1* showed a clear decrease in expression with age in males in snRNA-seq and ST (Fig. 8g). This highlighted the necessity to include both sexes when studying aging in the kidney.

Discussion

Sexual dimorphism is influenced by many factors⁵⁹ and is increasingly recognized for its role in kidney diseases and cancers⁶⁰. Here we have generated and integrated data from six platforms, producing the most comprehensive longitudinal multi-omic atlas and kidney sex difference study to date. PT has the most sex-biased gene expression, with substantial sex differences emerging after W3. We also observed sex-specific effects of aging, with the LOH, PT and CD being most differentially affected between the sexes. The broad integration of data over several dimensions, namely dissociative and spatial, RNA and protein, various resolutions and multiple time points, enabled a deep look at sex DEGs and sex-biased regulatory networks.

Our study revealed 227 and 164 respective genes having either male or female sex-biased expression and identified five spatial sex-biased patterns. The *Pigr* gene is associated with the transport and secretion of immunoglobulins in the immune system⁶¹, and *PIGR* is expressed by tubular scattered cells (TSCs) in healthy PT. Its expanded expression in injured kidneys⁶² is associated with elevated levels of urinary secretory immunoglobulin A, which are observed in patients with various kidney diseases⁶². Notably, our observation of heightened *Pigr* expression at the corticomedullary junction in male kidneys aligns with its susceptibility to injury^{61,63,64}, hinting at TSC enrichment in this region. A recent human study identified *PIGR* as a marker highly expressed in a subset of the PT population⁶⁵ and suggested this may be a putative cell of origin in some kidney cancers⁶⁵. Our analyses revealed that *Pigr*-expressing cells occupy the proximal portion of the PT(S3), constituting a clear molecular subdivision of this anatomically defined region of the kidney that may be relevant to the onset of kidney cancers and the higher incidence rate of ccRCC in males.

The unique spatial expression of *Cndp2* in the male cortex is also noteworthy. Its human ortholog *CNDP2* encodes carnosine dipeptidase 2, responsible for carnosine hydrolysis^{66,67}. Carnosine's antioxidant properties and ability to reduce proinflammatory cytokines⁶⁸ underscore its potential role in kidney health. SNPs in *CNDP1* and *CNDP2* are linked to an increased risk of diabetic nephropathy⁶⁶, further emphasizing the potential relevance of *Cndp2* in kidney disease susceptibility.

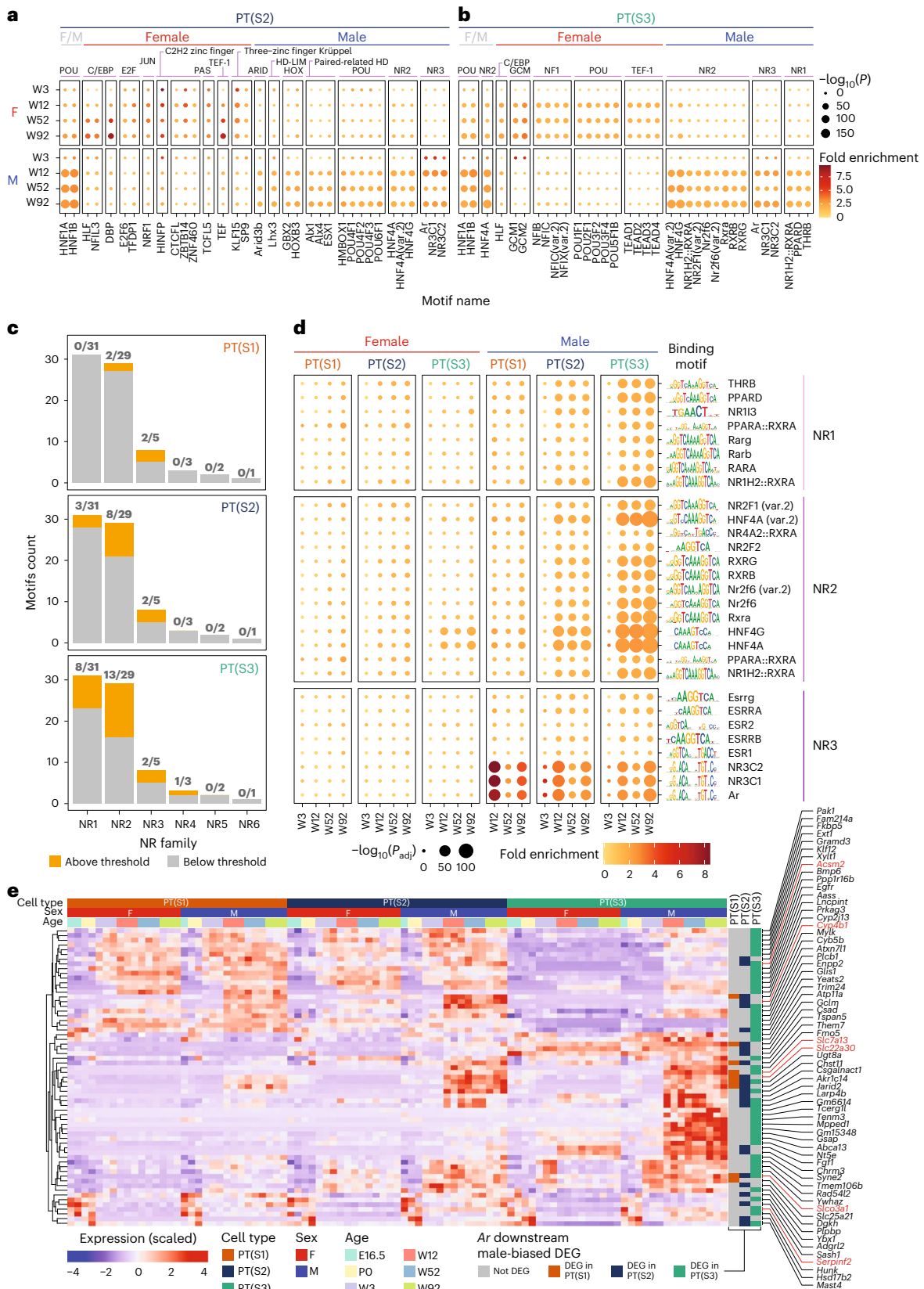


Fig. 6 | PT sex differences revealed by motif enrichment analysis. **a,b**, Overview of top motifs enriched in male- and female-specific peaks in PT(S2) (**a**) and PT(S3) (**b**). One-sided hypergeometric test was performed comparing the sex-biased peaks with randomly selected peaks with the same GC content. \log_{10} -transformed *P* value (Benjamini–Hochberg adjusted) is represented as the bubble size.

c, Number of motifs that are above or below threshold (with sex enrichment

patterns) for the NR motif family in PT segments (Methods). **d**, Overview of selected motifs from the NR family. Bubble size and color indicate adjusted *P* value and fold enrichment, respectively, given male- and female-specific peaks within each cell type and age. The *P* value calculation was done in the same way as explained in **a** and **b**. **e**, Heatmap showing the average expression of predicted downstream targets for the *Ar* motif in PT segments.

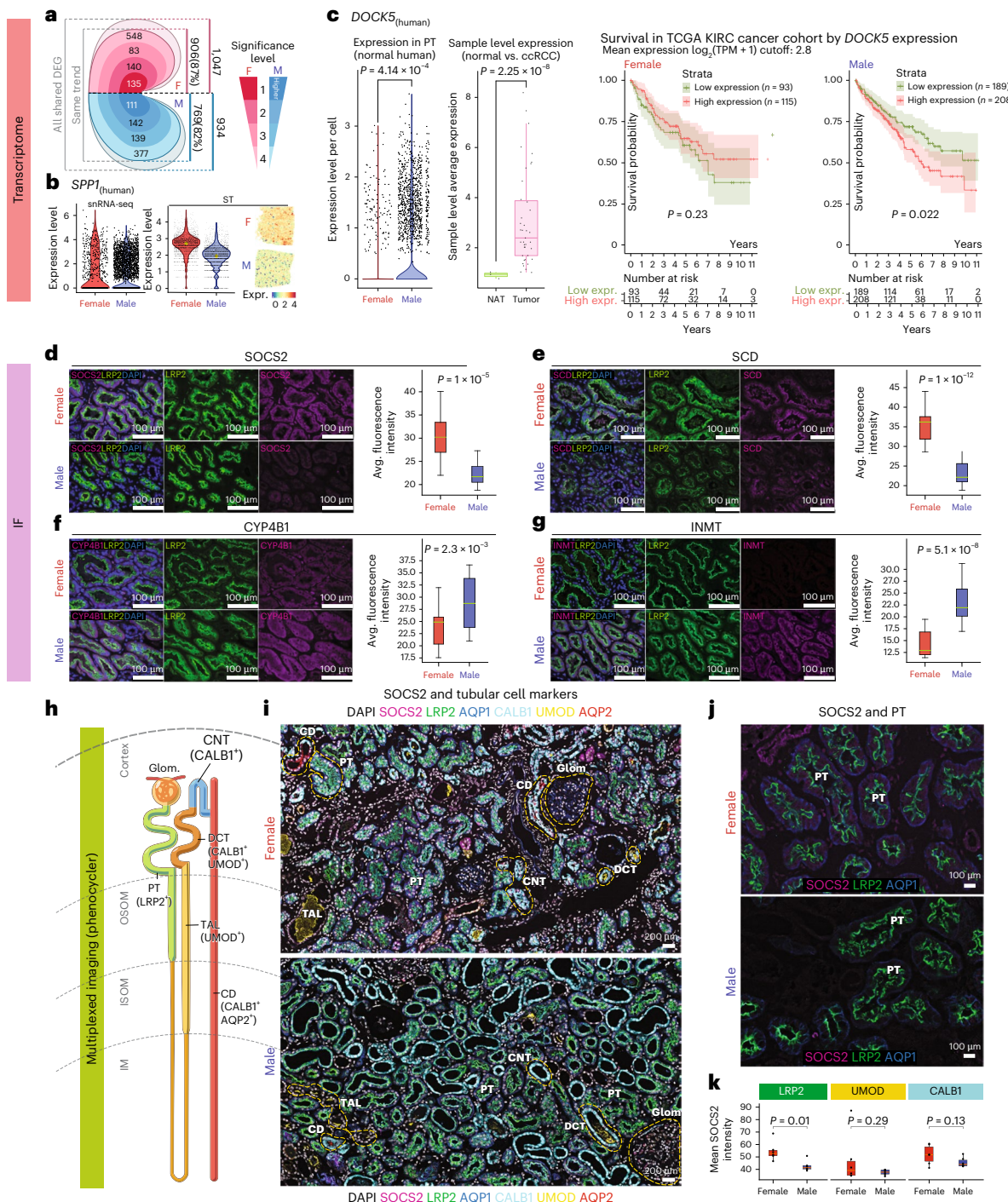


Fig. 7 | Sex DEG expression patterns in human kidneys. **a**, Diagram of overlapping male- and female-specific PT genes between mouse and human at various significance levels in human data (Methods; two-sided Wilcoxon rank-sum test Bonferroni method adjusted). **b**, Left, violin plot of *SPP1* snRNA expression in PT. Right, violin and spatial plots of *SPP1* expression from Visium ST. Yellow diamonds denote medians. **c**, Left, *DOCK5* expression in PT of normal human kidney samples (two-sided Wilcoxon rank-sum test). Middle, *DOCK5* expression in ccRCC tumor tissues compared to normal adjacent tissues. Boxplots show the median (centerline), first and third quartiles (hinges) and whiskers extending to values within $1.5 \times$ IQR from the hinges (two-sided Students' *t* test). Right, Kaplan–Meier curves of the survival status of patients based on low/high *DOCK5* expression, for males and females, separately (log-rank test). **d–g**, IF images and fluorescence intensity quantification of *SOCS2* (**d**), *SCD* (**e**), *CYP4B1* (**f**) and *INMT* (**g**) expression in female and male human kidney tissues (eight random areas, $n=3$). *LRP2* is used to label PT cells. Scale bar = 100 μ m.

Boxplots show the median (centerline), first and third quartiles (hinges) and whiskers extending to values within $1.5 \times$ IQR from the hinges (two-sided Welch's *t* test). Representative images of the three biological replicates are in Supplementary Figs. 4–7. **h**, Nephron structure diagram. **i**, CODEX images of *SOCS2*, *LRP2*, *AQP1*, *CALB1*, *UMOD* and *AQP2* in female and male human kidneys ($n=1$ for each sex for demonstration purpose). Scale bar = 200 μ m. **j**, CODEX images of *SOCS2*, *LRP2* and *AQP1* showing *SOCS2* difference of female versus male in human kidneys. Scale bar = 100 μ m. **k**, Mean *SOCS2* intensity in *LRP2*⁺, *UMOD*⁺ and *CALB1*⁺ cells. Boxplots show the median (centerline), first and third quartiles (hinges) and whiskers extending to values within $1.5 \times$ IQR from the hinges (two-sided Welch's *t* test). Quantification is performed on eight random regions from the multiplex image, repeated more than thrice with similar results. KIRC, kidney renal clear cell carcinoma; Expr, expression; Glom, glomeruli; IQR, interquartile range; TCGA, The Cancer Genome Atlas.

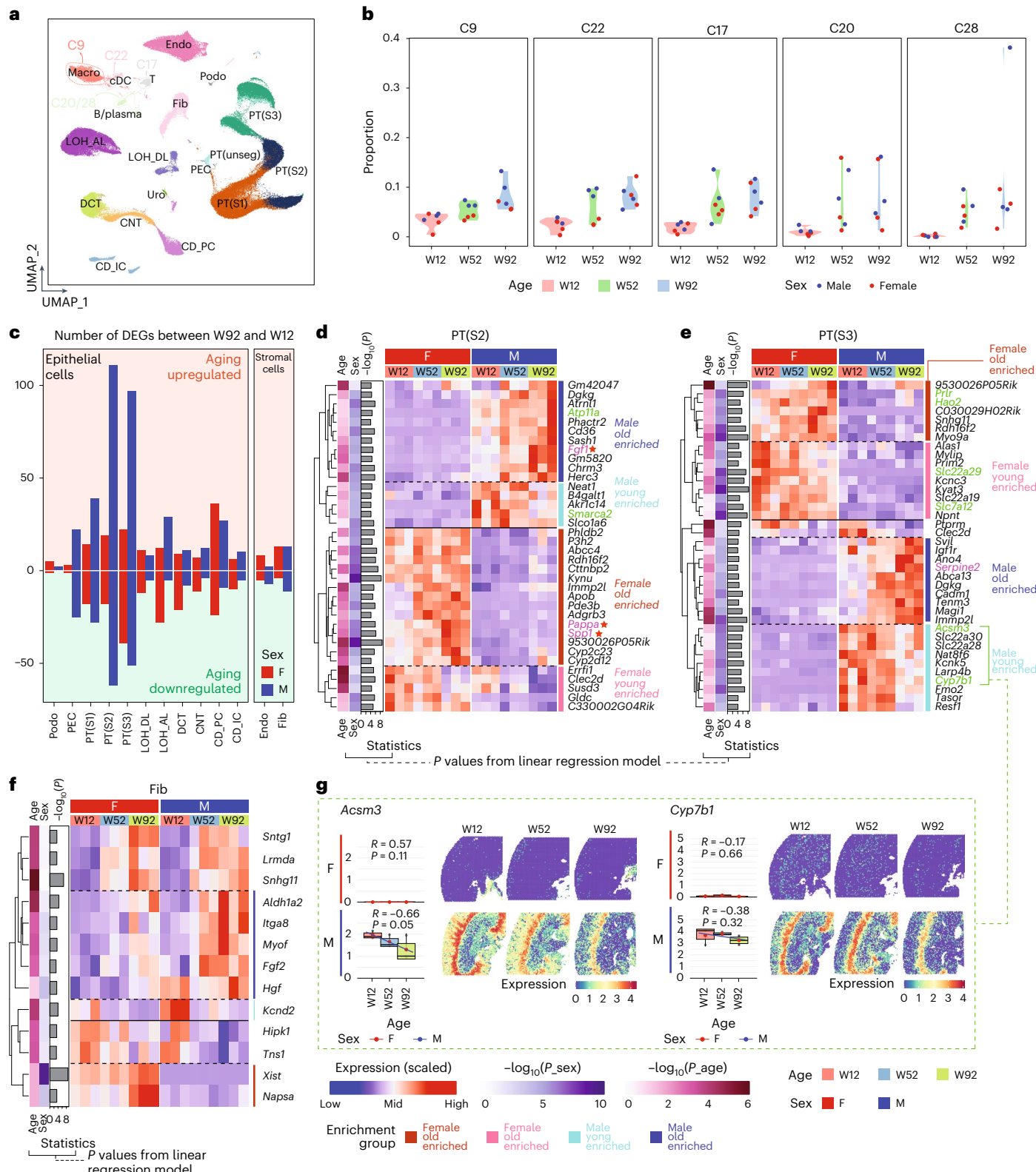


Fig. 8 | Aging in different kidney cell types. **a**, Cell-type distributions from adult kidneys based on multi-ome data. Colors represent cell types. **b**, Violin plot showing proportions of cells from clusters 9, 22, 17, 20 and 28 for each sample. **c**, Number of DEGs in major cell types comparing W92 to W12 samples in females and males, respectively. **d–f**, Heatmaps of top aging-associated DEGs in PT(S2) (**d**), PT(S3) (**e**) and Fib (**f**). Genes in purple are from the SenMayo list; genes in green are also sex DEGs from Fig. 3e; kidney disease-related genes are marked with red stars. Annotation bars on the left side indicate the \log_{10} -transformed P values from the linear regression model, expression ~ age + sex, that are

associated with age (two-sided Students' *t* test), sex (two-sided Students' *t* test) and the overall linear model (two-sided *F* test). Only genes with adjusted $P < 1 \times 10^{-10}$ and absolute $\log_{10}(FC) \geq 0.5$ in the W92–W12 differential expression testing (two-sided Wilcox, Bonferroni correction) were examined in this linear model, and no further multiple comparison adjustments were done. Color bars on the right denote the age-associated enrichment group of the genes. **g**, Expression of young male-enriched PT(S3) genes in snRNA-seq (left; $n = 3$ per age per sex; red dot indicates mean; Spearman correlation; two-sided *t* test) and ST (right).

Socs2, a female-biased DEG highlighted in our study, is reportedly induced by estrogen through estrogen receptor alpha (ER α)⁶⁹. Our regulon and motif enrichment analysis did not find evidence of direct ER regulation, consistent with previous work⁴. Conversely, we demonstrated that estrogen might indirectly control *Socs2* expression through prolactin, which activates the JAK2/STAT5 pathway for downstream *Socs2* activation. SOCS2 appears to suppress PRLR and JAK/STAT signaling⁷⁰, modulating multiple inflammatory cytokines and alleviating streptozotocin-induced kidney injury by inhibiting IL-1, IL-6, etc.⁷¹. JAK/STAT signaling is well known for immune responses⁷², and its activation is important during CKD pathogenesis⁷³.

Unlike ER in females, AR signaling appears to drive the expression of around 20% of the sex-biased DEGs we identified. Among these, *Serpinf2* is a potential serum marker for kidney injury, and its expression can be induced by testosterone in renal HEK293T cells⁷⁴. *Acsm2* is a sex-biased DEG in kidney PT^{4,35}, although our data suggested that it is controlled by androgen in kidney PT cells. *Acsm2* is also a kidney PT-specific gene, but its role in kidney diseases remains largely unknown³⁵. Our observations of AR regulation of sex-biased DEGs are consistent with the role of AR in establishing sex-dimorphic gene expression⁵. Our finding of PRLR/JAK/STAT involvement in regulating some female DEGs points toward a mechanistic explanation for the establishment of sex-dimorphic gene expression in the female kidney.

A common finding by us and others is that even ‘normal’ human kidney specimens tend to be genetically heterogeneous and show a wide range of age-, environmental- or disease-related histopathological changes. Despite these heterogeneities, we were able to see the same sex-biased gene expression in SOCS2, SCD, CYP4B1 and INMT in human kidneys. Our findings of SOCS2 in both mouse and human kidneys are reassuring and invite further investigation. In summary, this work strengthens our understanding of sex differences in normal kidneys with potential links to diseases such as AKI and ccRCC that disproportionately affect males.

Online content

Any methods, additional references, Nature Portfolio reporting summaries, source data, extended data, supplementary information, acknowledgements, peer review information; details of author contributions and competing interests; and statements of data and code availability are available at <https://doi.org/10.1038/s41588-025-02161-x>.

References

- McMahon, A. P. Development of the mammalian kidney. *Curr. Top. Dev. Biol.* **117**, 31–64 (2016).
- Ransick, A. et al. Single cell profiling reveals sex, lineage and regional diversity in the mouse kidney. *Dev. Cell* **51**, 399–413 (2019).
- Mayne, B. T. et al. Large scale gene expression meta-analysis reveals tissue-specific, sex-biased gene expression in humans. *Front. Genet.* **7**, 183 (2016).
- Chen, L., Chou, C.-L., Yang, C.-R. & Knepper, M. A. Multiomics analyses reveal sex differences in mouse renal proximal subsegments. *J. Am. Soc. Nephrol.* **34**, 829–845 (2023).
- Xiong, L. et al. Direct androgen receptor control of sexually dimorphic gene expression in the mammalian kidney. *Dev. Cell* **58**, 2338–2358 (2023).
- Huang, L. et al. Single-cell profiling reveals sex diversity in human renal proximal tubules. *Gene* **752**, 144790 (2020).
- Ide, S. et al. Sex differences in resilience to ferroptosis underlie sexual dimorphism in kidney injury and repair. *Cell Rep.* **41**, 111610 (2022).
- Kwekel, J. C., Desai, V. G., Moland, C. L., Vijay, V. & Fuscoe, J. C. Sex differences in kidney gene expression during the life cycle of F344 rats. *Biol. Sex Differ.* **4**, 14 (2013).
- Wu, H. et al. High resolution spatial profiling of kidney injury and repair using RNA hybridization-based *in situ* sequencing. *Nat. Commun.* **15**, 1396 (2024).
- McEvoy, C. M. et al. Single-cell profiling of healthy human kidney reveals features of sex-based transcriptional programs and tissue-specific immunity. *Nat. Commun.* **13**, 7634 (2022).
- Lu, Y.-A. et al. Sex-specific proximal tubular cell differentiation pathways identified by single-nucleus RNA sequencing. *Sci. Rep.* **14**, 24041 (2024).
- Hsu, R. K. et al. Exploring potential reasons for the temporal trend in dialysis-requiring AKI in the United States. *Clin. J. Am. Soc. Nephrol.* **11**, 14–20 (2016).
- Neugarten, J., Golestaneh, L. & Kolhe, N. V. Sex differences in acute kidney injury requiring dialysis. *BMC Nephrol.* **19**, 131 (2018).
- Peired, A. J. et al. Sex and gender differences in kidney cancer: clinical and experimental evidence. *Cancers* **13**, 4588 (2021).
- Sandberg, K. & Ji, H. Sex and the renin angiotensin system: implications for gender differences in the progression of kidney disease. *Adv. Ren. Replace. Ther.* **10**, 15–23 (2003).
- Colafella, K. M. M. & Denton, K. M. Sex-specific differences in hypertension and associated cardiovascular disease. *Nat. Rev. Nephrol.* **14**, 185–201 (2018).
- Miao, Z. et al. Single cell regulatory landscape of the mouse kidney highlights cellular differentiation programs and disease targets. *Nat. Commun.* **12**, 2277 (2021).
- Combes, A. N. et al. Single cell analysis of the developing mouse kidney provides deeper insight into marker gene expression and ligand–receptor crosstalk. *Development* **146**, dev178673 (2019).
- Young, M. D. et al. Single-cell transcriptomes from human kidneys reveal the cellular identity of renal tumors. *Science* **361**, 594–599 (2018).
- Stewart, B. J. et al. Spatiotemporal immune zonation of the human kidney. *Science* **365**, 1461–1466 (2019).
- Park, J. et al. Single-cell transcriptomics of the mouse kidney reveals potential cellular targets of kidney disease. *Science* **360**, 758–763 (2018).
- Wu, H., Kirita, Y., Donnelly, E. L. & Humphreys, B. D. Advantages of single-nucleus over single-cell RNA sequencing of adult kidney: rare cell types and novel cell states revealed in fibrosis. *J. Am. Soc. Nephrol.* **30**, 23–32 (2019).
- Muto, Y. et al. Single cell transcriptional and chromatin accessibility profiling redefine cellular heterogeneity in the adult human kidney. *Nat. Commun.* **12**, 2190 (2021).
- Wu, H. et al. Comparative analysis and refinement of human PSC-derived kidney organoid differentiation with single-cell transcriptomics. *Cell Stem Cell* **23**, 869–881 (2018).
- Lake, B. B. et al. An atlas of healthy and injured cell states and niches in the human kidney. *Nature* **619**, 585–594 (2023).
- Korsunsky, I. et al. Fast, sensitive and accurate integration of single-cell data with Harmony. *Nat. Methods* **16**, 1289–1296 (2019).
- Cable, D. M. et al. Robust decomposition of cell type mixtures in spatial transcriptomics. *Nat. Biotechnol.* **40**, 517–526 (2022).
- Vahid, M. R. et al. High-resolution alignment of single-cell and spatial transcriptomes with CytoSPACE. *Nat. Biotechnol.* **41**, 1543–1548 (2023).
- Wu, H. et al. Single-cell transcriptomics of a human kidney allograft biopsy specimen defines a diverse inflammatory response. *J. Am. Soc. Nephrol.* **29**, 2069–2080 (2018).
- Liberzon, A. et al. The Molecular Signatures Database (MSigDB) hallmark gene set collection. *Cell Syst.* **1**, 417–425 (2015).
- Fisher, J. L., Clark, A. D., Jones, E. F. & Lasseigne, B. N. Sex-biased gene expression and gene-regulatory networks of sex-biased adverse event drug targets and drug metabolism genes. *BMC Pharmacol. Toxicol.* **25**, 5 (2024).

32. Bell, M. R. Comparing postnatal development of gonadal hormones and associated social behaviors in rats, mice, and humans. *Endocrinology* **159**, 2596–2613 (2018).
33. LaCroix-Fralish, M. L., Tawfik, V. L. & DeLeo, J. A. The organizational and activational effects of sex hormones on tactile and thermal hypersensitivity following lumbar nerve root injury in male and female rats. *Pain* **114**, 71–80 (2005).
34. Maher, J. M., Cheng, X., Tanaka, Y., Scheffer, G. L. & Klaassen, C. D. Hormonal regulation of renal multidrug resistance-associated proteins 3 and 4 (Mrp3 and Mrp4) in mice. *Biochem. Pharmacol.* **71**, 1470–1478 (2006).
35. Watanabe, H. et al. Expression of *Acsm2*, a kidney-specific gene, parallels the function and maturation of proximal tubular cells. *Am. J. Physiol. Renal Physiol.* **319**, F603–F611 (2020).
36. Penalosa, C. G. et al. Sex-dependent regulation of cytochrome P450 family members Cyp1a1, Cyp2e1, and Cyp7b1 by methylation of DNA. *FASEB J.* **28**, 966–977 (2014).
37. Leung, K. C. et al. Estrogen inhibits GH signaling by suppressing GH-induced JAK2 phosphorylation, an effect mediated by SOCS-2. *Proc. Natl Acad. Sci. USA* **100**, 1016–1021 (2003).
38. Vergnes, L., Phan, J., Stoltz, A. & Reue, K. A cluster of eight hydroxysteroid dehydrogenase genes belonging to the aldo-keto reductase supergene family on mouse chromosome 13. *J. Lipid Res.* **44**, 503–511 (2003).
39. Sen, B. et al. STAT5A-mediated SOCS2 expression regulates Jak2 and STAT3 activity following c-Src inhibition in head and neck squamous carcinoma. *Clin. Cancer Res.* **18**, 127–139 (2012).
40. Radhakrishnan, A. et al. A pathway map of prolactin signaling. *J. Cell Commun. Signal.* **6**, 169–173 (2012).
41. LaPensee, C. R., Lin, G., Dent, A. L. & Schwartz, J. Deficiency of the transcriptional repressor B cell lymphoma 6 (Bcl6) is accompanied by dysregulated lipid metabolism. *PLoS ONE* **9**, e97090 (2014).
42. Meyer, R. D., Laz, E. V., Su, T. & Waxman, D. J. Male-specific hepatic Bcl6: growth hormone-induced block of transcription elongation in females and binding to target genes inversely coordinated with STAT5. *Mol. Endocrinol.* **23**, 1914–1926 (2009).
43. Morohoshi, K., Komatani, Y. & Harigaya, T. Estrogen induces phosphorylation of prolactin through p21-activated kinase 2 activation in the mouse pituitary gland. *J. Reprod. Dev.* **66**, 571–578 (2020).
44. Tsukahara, S., Kambe, F., Suganuma, N., Tomoda, Y. & Seo, H. Increase in Pit-1 mRNA is not required for the estrogen-induced expression of prolactin gene and lactotroph proliferation. *Endocr. J.* **41**, 579–584 (1994).
45. Zhang, Y., Laz, E. V. & Waxman, D. J. Dynamic, sex-differential STAT5 and BCL6 binding to sex-biased, growth hormone-regulated genes in adult mouse liver. *Mol. Cell. Biol.* **32**, 880–896 (2012).
46. Sehgal, P. B., Yang, Y.-M. & Miller, E. J. Hypothesis: neuroendocrine mechanisms (hypothalamus-growth hormone-STAT5 axis) contribute to sex bias in pulmonary hypertension. *Mol. Med.* **21**, 688–701 (2015).
47. Yang, Y.-M. & Sehgal, P. B. Smooth muscle-specific BCL6^{+/−} knockout abrogates sex bias in chronic hypoxia-induced pulmonary arterial hypertension in mice. *Int. J. Endocrinol.* **2018**, 3473105 (2018).
48. Weikum, E. R., Liu, X. & Ortlund, E. A. The nuclear receptor superfamily: a structural perspective. *Protein Sci.* **27**, 1876–1892 (2018).
49. Kaleta, B. The role of osteopontin in kidney diseases. *Inflamm. Res.* **68**, 93–102 (2019).
50. Liu, C. et al. Characterization of alternative splicing events in HPV-negative head and neck squamous cell carcinoma identifies an oncogenic DOCK5 variant. *Clin. Cancer Res.* **24**, 5123–5132 (2018).
51. Rajagopal, V. et al. Proteome-wide identification of RNA-dependent proteins in lung cancer cells. *Cancers* **14**, 6109 (2022).
52. Frank, S. R. et al. The focal adhesion-associated proteins DOCK5 and GIT2 comprise a rheostat in control of epithelial invasion. *Oncogene* **36**, 1816–1828 (2017).
53. Saul, D. et al. A new gene set identifies senescent cells and predicts senescence-associated pathways across tissues. *Nat. Commun.* **13**, 4827 (2022).
54. Coppé, J.-P., Desprez, P.-Y., Krtolica, A. & Campisi, J. The senescence-associated secretory phenotype: the dark side of tumor suppression. *Annu. Rev. Pathol.* **5**, 99–118 (2010).
55. Swindell, W. R., Masternak, M. M. & Bartke, A. In vivo analysis of gene expression in long-lived mice lacking the pregnancy-associated plasma protein A (*PappA*) gene. *Exp. Gerontol.* **45**, 366–374 (2010).
56. Eidi, M. & Ashjazadeh, L. Anti-urolithiatic effect of *Cucumis melo* L. var inodorous in male rats with kidney stones. *Urolithiasis* **51**, 45 (2023).
57. Hong, S.-Y. et al. Identification of the pivotal role of SPP1 in kidney stone disease based on multiple bioinformatics analysis. *BMC Med. Genomics* **15**, 7 (2022).
58. Shin, S., Srivastava, A., Alli, N. A. & Bandyopadhyay, B. C. Confounding risk factors and preventative measures driving nephrolithiasis global makeup. *World J. Nephrol.* **7**, 129–142 (2018).
59. Seifarth, J. E., McGowan, C. L. & Milne, K. J. Sex and life expectancy. *Gend. Med.* **9**, 390–401 (2012).
60. Merz, C. N. B. et al. Sex and the kidneys: current understanding and research opportunities. *Nat. Rev. Nephrol.* **15**, 776–783 (2019).
61. Andrianova, N. V. et al. Kidney cells regeneration: dedifferentiation of tubular epithelium, resident stem cells and possible niches for renal progenitors. *Int. J. Mol. Sci.* **20**, 6326 (2019).
62. Krawczyk, K. M. et al. Localization and regulation of polymeric Ig receptor in healthy and diseased human kidney. *Am. J. Pathol.* **189**, 1933–1944 (2019).
63. Spiegel, D. M., Shanley, P. F. & Molitoris, B. A. Mild ischemia predisposes the S3 segment to gentamicin toxicity. *Kidney Int.* **38**, 459–464 (1990).
64. Sekine, M. et al. Selective depletion of mouse kidney proximal straight tubule cells causes acute kidney injury. *Transgenic Res.* **21**, 51–62 (2012).
65. Zhang, Y. et al. Single-cell analyses of renal cell cancers reveal insights into tumor microenvironment, cell of origin, and therapy response. *Proc. Natl Acad. Sci. USA* **118**, e2103240118 (2021).
66. Ahluwalia, T. S., Lindholm, E. & Groop, L. C. Common variants in CNDP1 and CNDP2, and risk of nephropathy in type 2 diabetes. *Diabetologia* **54**, 2295–2302 (2011).
67. Teufel, M. et al. Sequence identification and characterization of human carnosinase and a closely related non-specific dipeptidase. *J. Biol. Chem.* **278**, 6521–6531 (2003).
68. Kilić-Pstrusinska, K. Carnosine and kidney diseases: what we currently know? *Curr. Med. Chem.* **27**, 1764–1781 (2020).
69. Leong, G. M. et al. Estrogen up-regulates hepatic expression of suppressors of cytokine signaling-2 and -3 in vivo and in vitro. *Endocrinology* **145**, 5525–5531 (2004).
70. Li, K. et al. SOCS2 regulation of growth hormone signaling requires a canonical interaction with phosphotyrosine. *Biosci. Rep.* **42**, BSR20221683 (2022).
71. Zhou, Y. et al. Suppressor of cytokine signaling (SOCS) 2 attenuates renal lesions in rats with diabetic nephropathy. *Acta Histochem.* **116**, 981–988 (2014).
72. Brosius, F. C. & He, J. C. JAK inhibition and progressive kidney disease. *Curr. Opin. Nephrol. Hypertens.* **24**, 88–95 (2015).
73. Marrero, M. B. et al. Direct stimulation of Jak/STAT pathway by the angiotensin II AT1 receptor. *Nature* **375**, 247–250 (1995).

74. Lu, Y. et al. Screening for potential serum biomarkers in rat mesangial proliferative nephritis. *Proteomics* **16**, 1015–1022 (2016).

Publisher's note Springer Nature remains neutral with regard to jurisdictional claims in published maps and institutional affiliations.

Open Access This article is licensed under a Creative Commons Attribution-NonCommercial-NoDerivatives 4.0 International License, which permits any non-commercial use, sharing, distribution and reproduction in any medium or format, as long as you give appropriate credit to the original author(s) and the source, provide a link to the

Creative Commons licence, and indicate if you modified the licensed material. You do not have permission under this licence to share adapted material derived from this article or parts of it. The images or other third party material in this article are included in the article's Creative Commons licence, unless indicated otherwise in a credit line to the material. If material is not included in the article's Creative Commons licence and your intended use is not permitted by statutory regulation or exceeds the permitted use, you will need to obtain permission directly from the copyright holder. To view a copy of this licence, visit <http://creativecommons.org/licenses/by-nc-nd/4.0/>.

© The Author(s) 2025

¹Department of Medicine, Washington University in St. Louis, St. Louis, MO, USA. ²McDonnell Genome Institute, Washington University in St. Louis, St. Louis, MO, USA. ³Department of Mechanical Engineering and Materials Science, Washington University in St. Louis, St. Louis, MO, USA. ⁴Department of Surgery, Washington University in St. Louis, St. Louis, MO, USA. ⁵Department of Pathology and Immunology, Washington University in St. Louis, St. Louis, MO, USA. ⁶Department of Paediatrics, Washington University School of Medicine St Louis, St. Louis, MO, USA. ⁷Department of Neuroscience, Washington University School of Medicine St Louis, St. Louis, MO, USA. ⁸Samuel Oschin Comprehensive Cancer Institute, Department of Medicine, Department of Biomedical Sciences, Cedars-Sinai Medical Center, Los Angeles, CA, USA. ⁹Department of Cell Biology and Physiology, Washington University School of Medicine, St Louis, MO, USA. ¹⁰Siteman Cancer Center, Washington University in St. Louis, St. Louis, MO, USA. ¹¹Department of Genetics, Washington University in St. Louis, St. Louis, MO, USA. ¹²These authors contributed equally: Siqi Chen, Ruiyang Liu, Chia-Kuei Mo. ✉ e-mail: lding@wustl.edu; fchen@wustl.edu

Methods

Mouse strains, embryo staging and sample processing

All animal experiments were approved by the Washington University in Saint Louis Institutional Animal Care and Use Committee office. We used W3, W12, W52 and W92 C57BL/6J mice (strain 000664), which were purchased from the Jackson Laboratory. We inbred C57BL/6J mice (strain 000664), which were purchased from the Jackson Laboratory to get E16.5 and P0 mice in-house with a temperature range from 68 °F to 79 °F (20–26 °C), the humidity of 30–70% and a diurnal cycle light (dark cycle of 12 h on and 12 h off). To get E16.5 kidneys, four female mice and one male mouse were grouped for mating on day 1 at 5 pm. Then the male was removed from the females on day 2 at 10 am. Day 2 was designated as E0.5 for any pregnant females. For other ages, mice were purchased from the Jackson Laboratory. Mice at E16.5 and P0 were killed by decapitation. Older mice were killed by carbon dioxide asphyxiation. For each mouse, one kidney was embedded in optimal cutting temperature (OCT) compound, and the other one was fixed in 10% neutral buffered formalin (Epredia, 5725) and then embedded in paraffin. For Visium ST, 10 µm midsagittal OCT sections were used on the 10× Genomics Visium platform; for snRNA-seq and snATAC-seq, pooled snap-frozen tissues were used for E16.5 and P0 mice, and 300 µm of midsagittal OCT sections were used for mice from W3 to W92.

Human specimens

All human samples from our institution were collected with written informed consent in concordance with institutional review board (IRB) approval at Washington University in St. Louis (IRB protocol 201411135). Normal adjacent tissue samples were collected during surgical resection of renal cell carcinoma and verified by standard pathology. Two pairs (male and female) of normal human kidney formalin-fixed, paraffin-embedded (FFPE) blocks were purchased from AMSBIO (<https://www.amsbio.com/>) and Origene (<https://www.origene.com/>). Samples for snRNA-seq analysis were downloaded from the Kidney Precision Medicine Project (<https://cellxgene.cziscience.com/collections/bcb61471-2a44-4d00-a0af-ff085512674c>). Detailed information is listed in Supplementary Table 4.

Sex determination for mouse embryos

PCR was used to confirm the sex of E16.5 embryos. DNA from a small piece of the tail was isolated and used for PCR genotyping using the Promega GoTaq Flexi DNA Polymerase Kit with 1 µl Primer Mix (25 pmol µl⁻¹ of SRYF and 25 pmol µl⁻¹ SRYR). Primer sequences are listed in Supplementary Table 6. PCR began by heating at 94 °C for 2 min, followed by 40 cycles (94 °C for 20 s, 58.5 °C for 30 s and 72 °C for 30 s) in a Bio-Rad C1000PCR Thermal Cycler. The amplified DNA from test samples along with the male and female control samples was visualized on 1.5% agarose gels in the tris-acetate-EDTA (TAE) buffer. Male samples showed a 273-bp band for the SRY gene, and females showed no bands.

Single nuclei library preparation and sequencing

As previously described in ref. 75, nuclei lysis buffer was freshly prepared in cold nuclease-free water with a mixture of 10 mM Tris-HCl (pH 7.4; Thermo Fisher Scientific, 15567027), 10 mM NaCl (Thermo Fisher Scientific, AM9759), 3 mM MgCl₂ (Thermo Fisher Scientific, AM9530G), 0.01% NP40 substitute (Sigma, 74385-1L), 1% BSA (MACS, 130-091-376), 1 mM dithiothreitol (DTT) (Sigma, 646563) and 0.4 U µl⁻¹ Protector RNase inhibitor (Sigma, 3335402001). Cryopreserved tissues were lysed and filtered through a 40 µm strainer and washed with the wash buffer (2% BSA + 1× PBS + 0.4 U µl⁻¹ Protector RNase Inhibitor). The filtrate was resuspended in 500 µl wash buffer for fluorescence-activated cell sorting. Nuclei were stained with 7-aminoactinomycin D dye (Millipore Sigma, SML1633-1ML) at a 1:200 dilution for sorting 400,000 positively stained nuclei. The sorted nuclei were resuspended in 2× nuclei dilution buffer

(10x Genomics, 2000153) supplemented with 1 M DTT and 1.2 U µl⁻¹ protector RNase inhibitor. Nuclei were stained with Trypan blue (0.4%; Invitrogen, T10282) and quantified using a hemocytometer. In total, 20,000 nuclei were transposed and partitioned into gel beads-in-emulsion (GEMs) in the Chromium Controller (10x Genomics) and made into libraries following the Chromium Next GEM Single Cell Multiome ATAC + Gene Expression protocol CG000338 Rev A (10x Genomics). All libraries were sequenced on the Illumina NovaSeq 6000 system with specific flow cell types (snRNA-seq-S4; snATAC-seq-S1).

Mouse/human ST library preparation and sequencing

Fresh mouse kidneys were embedded with OCT on dry ice. OCT-embedded tissues sectioned at 10 µm thickness were then placed on the Visium Spatial Gene Expression Slide following the Visium Spatial Protocols-Tissue Preparation Guide (10x Genomics, CG000240 Rev A). Visium ST libraries were constructed following the Visium Spatial Gene Expression Reagent Kits User Guide CG000239 Rev A (10x Genomics). Libraries were sequenced on the S4 flow cell of the Illumina NovaSeq 6000 system. Human kidney tissues were acquired from OriGene and followed the same procedure.

Mouse Xenium library preparation, imaging and data analysis

Freshly procured mouse kidneys were fixed and embedded into paraffin blocks (FFPE blocks). Kidneys were processed following the FFPE Tissue Preparation Guide (10x Genomics, CG000578, Rev B). Overnight *in situ* probe hybridization was performed using 379 probes from the Xenium Mouse Tissue Atlassing Panel (10x Genomics, 1000627) plus an additional 100 custom probes (Supplementary Table 3). Probe ligation, rolling circle amplification, background quenching and nuclei staining were done following the protocol (10x Genomics, CG000582, Rev D). Samples, buffers and decoding consumables were loaded into the Xenium analyzer (10x Genomics, 1000481). The run was initialized using the guidance provided (10x Genomics, CG000584, Rev C). These fluorescent reporters hybridized to targeted complementary regions of the barcoded circularized cDNA were imaged. Hematoxylin and eosin (H&E) stain was performed on the same region after the run was complete.

Mouse Xenium image alignment and data analysis

As previously described in ref. 75, H&E images were integrated with Xenium data using the manual Image Alignment workflow from Xenium Explorer 1.3.0 (Image Alignment in Xenium Explorer from the 10x Genomics Xenium Tutorial Page, <https://www.10xgenomics.com/support/software/xenium-explorer/latest/tutorials/xe-image-alignment>). Cell types were assigned by reviewing the top DEGs of each unsupervised cluster, confirming their anatomical locations and/or reviewing morphological structure with the aligned H&E image. Kidney zones were assigned based on H&E images. Samples from both sexes were set to the same scale per gene to allow cross-sample comparison. To generate an expression trend plot from cortex to IM, we first take a rectangular crop in the middle of the sample, divide the x axis into 50 bins, calculate the average expression in each bin and then create the expression trend plot based on their location on the x axis.

Multi-ome data alignment

Reads from Chromium libraries were demultiplexed using bcl2fastq-v2.20 to obtain raw FASTQ files. Then, the raw FASTQ files were aligned and quantified with software CellRanger-ARC (v2.0.0) using the mouse reference genome (mm10). The resulting gene and fragment count matrices for each sample were treated as input for downstream analysis.

Joint analysis of snRNA-seq and snATAC-seq modality from multi-ome data

The RNA and ATAC assays from multi-ome datasets were first integrated separately using the R package Harmony²⁶ (v0.1.0). A batch is defined

by the nuclei dissociation date for samples that are processed together using the 10x Genomics Single Cell Multiome protocol (Supplementary Table 1). For batch effect correction, the function RunHarmony was applied for latent semantic index (LSI) components. The barcodes that passed both snRNA and snATAC quality control filters were kept for a joint analysis. Briefly, TF-IDF normalization of the peak-count matrix was performed, followed by LSI-dimensional reduction using the RunTFIDF and RunSVD Signac (v.1.5.0) functions. For normalization and dimensional reduction of the gene-count matrix, we used the SCTransform and RunPCA functions of Seurat (v4.1.1) with the same parameters as were used for regular scRNA-seq/snRNA-seq data processing. Next, the weighted nearest neighbor (WNN) graph was computed with the FindMultiModalNeighbors function using both data modalities. The 1:50 principal component analysis (PCA) components from snRNA-seq and 2:50 LSI components from snATAC-seq were used for this analysis. Nonlinear dimensionality reduction of the resulting WNN graph was performed using the RunUMAP function from Seurat. Finally, clusters with the FindClusters function were obtained using the WNN graph, setting the argument algorithm = 3 (SLM).

Cell-type annotation

Cell-type assignment was done based on known markers from literature and publicly available databases^{17,18,29,30} (<http://humphreyslab.com/SingleCell/>). To separate S1/S2/S3 segments within PT, we cross-checked the top cluster-specific genes within the PT population with the dataset from ref. 4, which consisted of bulk RNA data for PT-S1/PT-S2/PT-S3, separately, for both male and female mice.

SoupX-based ambient RNA removal and evaluation

R package SoupX²⁶ (v1.6.2) was used for estimating the impact of ambient RNA on data quality. To evaluate the results from SoupX, top cell-type-specific genes were obtained for each sample when processed either with or without ambient RNA removal. For each sample, the top 20 cell-type-specific genes were used for each cell type with or without ambient RNA removal to calculate the expression correlation among cell types before and after ambient RNA removal. The results suggest that there were no obvious differences in terms of expression profiles before and after ambient RNA removal (as shown in Supplementary Fig. 3).

Human snRNA data analysis

For human snRNA-seq, processed and annotated R data object was downloaded from the Kidney Precision Medicine Project (KPMP; <https://cellxgene.cziscience.com/collections/bcb61471-2a44-4d00-a0af-ff085512674c>). Samples within the object were further filtered based on the following parameters: (1) donors are without AKI/CKD, (2) samples are prepared from nuclei and (3) donors are Caucasian under the age of 60. Six samples (four females and two males) remained and were used for the downstream differential expression analysis. For Fig. 7a, mouse DEGs whose percentage of expression in human data is below 10% are discarded; the number of the remaining genes is represented in the outermost circles. Within the outermost circles are the human sex DEGs with the same trend as mouse data. Among the overlapping genes, the following different levels of differential expression are defined from the human data side: level 1—the absolute value of log-transformed fold change (FC) no smaller than 1, and adjusted *P* value smaller than 0.05; level 2—the absolute value of log-transformed FC between 0.5 and 1, and adjusted *P* value smaller than 0.05; level 3—the absolute value of log-transformed FC between 0.25 and 0.5, and adjusted *P* value smaller than 0.05; and level 4—other genes that show the same trend across mouse and human.

Group correlation analysis

For group correlation analysis as shown in Extended Data Fig. 5, the correlation for the average expression/average peak accessibility was

calculated for each age, sex and cell type. The top 20 cell-type-specific genes/peaks from each sample were taken out as the feature set used for correlation.

Sex-based differential expression analysis

Differential expression analysis for snRNA-seq/snATAC-seq was conducted using the Seurat function FindMarkers. A gene is determined as ‘sex-biased’ in a given age and a given segment if $\log_2(\text{FC}) > 0.5$ and $P_{\text{adj}} < 1 \times 10^{-50}$. DEG analysis compared PT(S2) and PT(S3) expression between males and females at each age using snRNA and Visium ST. Candidate DEGs (Fig. 3e and Extended Data Fig. 6c) met the following criteria: (1) consistent FC trends in snRNA and Visium ST, (2) a ranking difference of at least 150 between sexes of the same age and (3) absolute $\log(\text{FC}) > 1.5$ in snRNA or Visium ST. The average expression of heatmap genes was calculated using AverageExpression ('slot' set to 'data') and scaled across time points for visualization. In the human study, male–female comparisons for each cell type used Seurat's FindMarkers. For human/mouse DEG overlap analysis, mouse DEGs were identified in PT segments at W12 or W52. The corresponding human genes were then tested for sex differences. Genes with expression below 10% were excluded from the analysis. Genes were classified into four levels based on stringency (levels 1–4). Levels 1–3 required $P_{\text{adj}} < 0.05$, with absolute $\log(\text{FC}) \geq 1$ (level 1), 0.5–1 (level 2) and 0.25–0.5 (level 3). Level 4 included genes identified by FindMarker but not in levels 1–3. Overlapping genes with consistent sex difference trends across humans and mice were counted for each level (Fig. 6a).

Age-based differential expression analysis

Age-based differential expression analysis included two approaches. First, for each cell type and sex, DE was assessed between W92 and W12. Candidate genes had $P_{\text{adj}} < 1 \times 10^{-10}$ and absolute $\log(\text{FC}) \geq 0.5$. In addition, genes from the SenMayo senescence signature were included in the second analysis, focusing on the candidate genes. We applied linear regression to model the average gene expression for each sample over age and sex for each cell type of interest (given a specific cell type, the sample-level average gene expression – age + sex, where the ages in this linear model include W12, W52 and W92). Heatmap candidate aging-associated genes from PT(S2)/PT(S3) had $P < 1 \times 10^{-4}$ in the linear model (Fig. 7e–h). For fibroblasts, the *P* value cutoff was set as 1×10^{-3} .

Gene-set enrichment analysis (GSEA)

For pathway analysis of sex-biased genes (Fig. 3a,b), human orthologs of mouse genes were identified using an online mapping tool, g:Orth, from the g:Profiler²⁷ and then used function GSEA (package—clusterProfiler v3.18.1) to obtain the normalized enrichment score of Hallmark pathways (package—msigdbr v7.5.1) from the MSigDB³⁰ on the PT(S3) sex-biased genes. For visualization in Fig. 3b, we focused on pathways with consistent sex-biased enrichment across adult mouse kidneys (W12–W92). The final genes and pathways displayed in Fig. 3b passed the following filtering thresholds to reflect the core enrichment components: (1) expression-based filtering—a gene must be a significant sex-biased DEG ($\text{avg_log}_2(\text{FC}) > 0.5$ and Bonferroni adjusted $P < 0.01$) in all three adult time points; (2) Gene-level enrichment score (GES)-based pathway filtering—a pathway must have more than ten core enrichment genes with $\text{GES} > 0.5$. GES is defined as $\text{GES}_{\text{pathway},\text{gene}} = \text{NES}_{\text{pathway}} * \text{Expression}_{\text{gene}}$. NES, normalized enrichment score.

Regulon analysis

The R package SCENIC (v1.2.4) was used for regulon analysis²⁸. For each sample (E16.5–W92), up to 100 cells from PT(S1), PT(S2) and PT(S3) were randomly sampled for SCENIC analysis. The analysis followed the online tutorial with default parameters. Sex separation was found in cells starting from W12 shown in the tSNE plot. Therefore, we mainly focused on cells from W12, W52 and W92 for the downstream analysis.

The selection criteria for finding segment-specific regulons (as shown in Fig. 4a) are described below. Among all the regulons, for each age, we did a Wilcoxon test by comparing the binary activity from a specific PT segment and the rest of the PT segments. For each segment, only regulons with $P < 0.01$ and higher average binary activities than the other segments (W12–W92) were carried to the next step. Then, among the candidates found above, we calculated the group average binary activity (each group represented a cell type from a specific sample), and only the regulons whose maximum average activity among groups was greater than 0.4 were taken for visualization in Fig. 4a.

Motif annotation and score calculation

ChromVAR (v1.16.0)⁷⁹ was used to evaluate TF binding accessibility profiles in the snATAC-seq data. We used 724 motif position weight matrices from the JASPAR 2020 CORE vertebrates database⁸⁰ (v0.99.10) to run chromVAR with the default parameters. The matchMotifs function from the package motifmatchr was used to annotate whether peaks from snATAC data contained a specific motif. To then calculate motif scores given a group of cells, the motif score for each individual barcode was first extracted using the function GetAssayData when the default assay is set as ‘chromvar’. The motif score of a specific group of cells was calculated as the average of the motif scores from the individual cells.

Motif enrichment analysis

DARs within each segment were obtained using the function FindMarkers with logistic regression as the testing method (`logfc.threshold = 0.1, min.pct = 0`). Male-/female-specific DARs were defined as a group of peaks with an expected trend whose adjusted P value was below 0.05. The 5,0000 peaks that fell within open peaks were randomly sampled from the same age, cell type and sex with the same GC contents as the background. The function FindMotifs was then used to find enriched motifs given the sets of query and background peaks (Source Data Fig. 6). For the ‘above threshold’ motifs shown in Fig. 6c, the threshold is defined as follows: the enrichment score is at least 1.5 and $P_{adj} < 1 \times 10^{-10}$, for at least one of the time points among W12, W52 and W92, for either male or female, within each PT segment.

Visium ST data analysis

As previously described in ref. 75, after cDNA library construction and sequencing, the read alignment algorithm ‘count’ method in Space Ranger (v1.3.0) from the 10x Genomics was used to align reads to the mouse reference genome (mm10, 2020A). The resulting count matrix and associated H&E physiological images were then used by the R package Seurat (v.4.0.4) for subsequent analysis. The filtered gene-count matrices of all samples were normalized using SCTransform before being merged into one object for joint processing and analysis using the FindNeighbors and FindClusters function in Seurat using standard processing parameters (30 PCs, original Louvain algorithm). Cell-type composition of spots in the Visium ST data was deconvoluted using cell-type assignment in snRNA-seq samples of the same age and sex using the RCTD deconvolution algorithm.

Cell-type mapping and deconvolution of Visium ST data

Cell-type composition per spot was deconvolved using RCTD²⁷ (v2.0.0) using default parameters and `doublet_mode = ‘full’`. The reference of each run uses single-cell-level cell-type assignments from snRNA-seq data of the same age and sex. For example, processed and combined male W3 snRNA-seq objects were used to deconvolve cell types in ST samples of the same age and sex. In addition, we used the cell-type mapping and deconvolution tool CytoSPACE (v1.0.3)²⁸ to both deconvolve cell types in each spot and to infer the spatial location of cells in snRNA-seq data. We again used default parameters and matching ST data for the mapping. CytoSPACE mapping results were used in Fig. 1a for visualization of spatial cell-type distribution.

IF and microscopy

Fresh tissues were fixed in 10% neutral buffered formalin (Epredia, 5725) at room temperature overnight. Tissues were then dehydrated, infiltrated with wax and embedded into paraffin blocks. After tissues were processed into FFPE blocks, 5 μ m sections were cut and placed on glass slides. Next, sections were deparaffinized and rehydrated, followed by antigen retrieval using Tris EDTA buffer at pH 9 (Genemed, 10-0046) or 1× sodium citrate at pH 6 (Sigma, C9999) according to the manufacturer’s recommendation for specific antibodies. Then, sections were blocked with 100 mM glycine for 20 min, followed by blocking with 10% normal serum and 1% BSA for 1 h at room temperature. A negative control and a secondary antibody control were used in each experimental setting. Primary antibodies used are SOCS2 (Invitrogen, 34-6900; 1:50), AKR1C1 (orthologous to mouse AKR1C21; LSBio, LS-B15860-200; 1:100), INMT (Invitrogen, PA5-97875; 1:100), SCD (orthologous to mouse SCD1; Invitrogen, MA1-26155; 1:50), CYP4B1 (Invitrogen, PA5-106560; 1:100) and LRP2 (Abcam, ab76969; 1:1,000). Secondary antibodies used are Alexa Fluor Plus 594 (Invitrogen, 32754; 1:1,000), Alexa Fluor Plus 647 (Invitrogen, 32795; 1:1,000), Alexa Fluor Plus 647 (Invitrogen, 32787; 1:1,000), Alexa Fluor 488 (Invitrogen, 21206; 1:1,000) and LTL (Vector Labs, FL1321; 1:300). Images were collected by a Leica DMi8 microscope.

IF quantification

Images were cropped to their first 1,067 lines, and then LRP2 was processed to generate a mask for the quantification of SOCS2, INMT, SCD and CYP4B1 as follows: (1) a grayscale seed image of the same resolution of LRP2 and uniform intensity of 255 was created; (2) all image border pixels of both LRP2 and the seed were set to 0; (3) a morphological reconstruction by erosion of LRP2 was performed by executing `skimage.morphology.reconstruction` from the Python package scikit-image (v.0.19.0); (4) each pixel of LRP2 was subtracted from the corresponding pixel of the resulting image, and the result was binarized where all nonzero pixels were set to 0 and all other pixels were set to 1; (5) LRP2 was binarized where all pixels above a threshold (10 for INMT and 15 for the others) were set to 1 and all other pixels were set to 0; (6) finally, the mask was generated by multiplying both binarized images. For each image, the mean expression of the target gene was calculated considering only positive masked pixels. Their results were then grouped with boxplots, and the P value between females and males was calculated for each gene. Measurements were taken from three distinct samples.

Multiplexed IF staining and imaging

A panel of 22 PhenoCycler antibodies (Supplementary Table 5) was designed for human kidneys. This panel includes LRP2 and AQP1, UMOD and CALB1. Carrier-free antibodies were verified for their specificity by using IF staining in multiple channels. Once verified, antibodies were conjugated using the Akoya Antibody Conjugation Kit (Akoya Biosciences, SKU 7000009) with a barcode (Akoya Biosciences) assigned based on the IF staining results. Several common markers were directly purchased through Akoya Biosciences. PhenoCycler staining and imaging were performed according to the manufacturer’s instructions (PhenoCycler User Manual—Rev C). Imaging of the PhenoCycler multicycle experiment was performed using Keyence fluorescence microscope (model BZ-X810) equipped with a Nikon CFI Plan Apo λ $\times 20/0.75$ objective, the PhenoCycler instrument (Akoya Biosciences) and the PhenoCycler Instrument Manager (Akoya Biosciences). The raw images were then stitched and processed using the PhenoCycler processor (Akoya Biosciences). After multiplexed imaging was completed, H&E staining was performed on the same tissue.

Multiplexed imaging quantification

Six nonoverlapping regions of resolution 4k by 4k pixels were cropped from each PhenoCycler sample, and their pixel values were converted to eight bits. A mask for the quantification of SOCS2 was generated as previously described in the IF quantification section (threshold

adjusted to 30). The quantification was then performed as described in the same 'IF quantification' section. The same was performed for UMOD and for CALB1, instead of LRP2.

Statistics and reproducibility

In this study, we exclusively used mice from C57BL/6J, an inbred subline for which variance is known to be low. Samples of $n = 3$ mice per sex per group were chosen based upon well-established empirics from prior studies^{81–83} establishing this as a suitable sample size. No data were excluded from the analyses. The mice were either randomly sent from Jackson Laboratory or randomly inbred in-house, then randomly allocated into experimental groups. The investigators were not blinded to allocation during experiments and outcome assessment. Each experiment was repeated independently at least three times.

Reporting summary

Further information on research design is available in the Nature Portfolio Reporting Summary linked to this article.

Data availability

Raw data for multi-ome and Visium have been deposited into Gene Expression Omnibus (GEO)—[GSE252772](#). Raw and processed data for Xenum have been deposited into GEO—[GSE286051](#). Source data are provided with this paper.

Code availability

All bioinformatics programs used in this study are available from https://github.com/ding-lab/normal_mouse_kidney_scripts at the GitHub public repository⁸⁴. A Shiny web app to visualize Visium cell types and spatial gene expression is available at https://cmowustl.shinyapps.io/shiny_st/.

References

75. Mo, C.-K. et al. Tumour evolution and microenvironment interactions in 2D and 3D space. *Nature* **634**, 1178–1186 (2024).
76. Young, M. D. & Behjati, S. SoupX removes ambient RNA contamination from droplet-based single-cell RNA sequencing data. *Gigascience* **9**, giaa151 (2020).
77. Raudvere, U. et al. g:Profiler: a web server for functional enrichment analysis and conversions of gene lists (2019 update). *Nucleic Acids Res.* **47**, W191–W198 (2019).
78. Aibar, S. et al. SCENIC: single-cell regulatory network inference and clustering. *Nat. Methods* **14**, 1083–1086 (2017).
79. Schep, A. N., Wu, B., Buenrostro, J. D. & Greenleaf, W. J. chromVAR: inferring transcription-factor-associated accessibility from single-cell epigenomic data. *Nat. Methods* **14**, 975–978 (2017).
80. Fornes, O. et al. JASPAR 2020: update of the open-access database of transcription factor binding profiles. *Nucleic Acids Res.* **48**, D87–D92 (2020).
81. Sheng, M. H.-C., Lau, K.-H. W., Beamer, W. G., Baylink, D. J. & Wergedal, J. E. In vivo and in vitro evidence that the high osteoblastic activity in C3H/HeJ mice compared to C57BL/6J mice is intrinsic to bone cells. *Bone* **35**, 711–719 (2004).

82. Leduc, M. S. et al. A major X-linked locus affects kidney function in mice. *Mol. Genet. Genomics* **287**, 845–854 (2012).
83. Scarfe, L. et al. Long-term outcomes in mouse models of ischemia-reperfusion-induced acute kidney injury. *Am. J. Physiol. Ren. Physiol.* **317**, F1068–F1080 (2019).
84. RuiyangLiu94. ding-lab/normal_mouse_kidney_scripts: multi-omic and spatial analysis of mouse kidneys highlights sex-specific differences in gene regulation across the lifespan (kidney). Zenodo <https://doi.org/10.5281/zenodo.14962669> (2025).

Acknowledgements

This study has been supported in part by the National Institute of Diabetes and Digestive and Kidney Diseases (U01DK3380 to F.C. and L.D.) and National Institutes of Health Common Fund award (U54AG075934 to L.D., F.C. and S.A.S.). We thank the Genome Technology Access Center at the McDonnell Genome Institute at Washington University School of Medicine for help with some of the sequencing work. We thank HuBMAP (U54HL45608) and KPMP consortia for the availability of the reference atlas data on the CellxGene portal. The authors would like to thank I. Strunilin and A. Southard-Smith for their critical review of the manuscript.

Author contributions

L.D. and F.C. conceptualized and designed the project. S.C., P.L., Y.Z. and M.N.A. collected mouse samples. S.C., A.H., P.L., Y.Z., W.C., A.T.S., A.A.-D., N.N.A.L.D., K.S., Xiang Li, J.M.H. and S.J. developed and performed experiments or data collection. R.L., C.M., M.C.W., A.L.N.T.C., Y.L. and A.K. carried out computation and statistical analysis. S.C., R.L., C.M., L.D. and F.C. carried out data interpretation and biological analyses. S.C., R.L., C.M., M.C.W., J.B.R., Xue Li, S.A.S., L.D. and F.C. did the writing of the manuscript.

Competing interests

The authors declare no competing interests.

Additional information

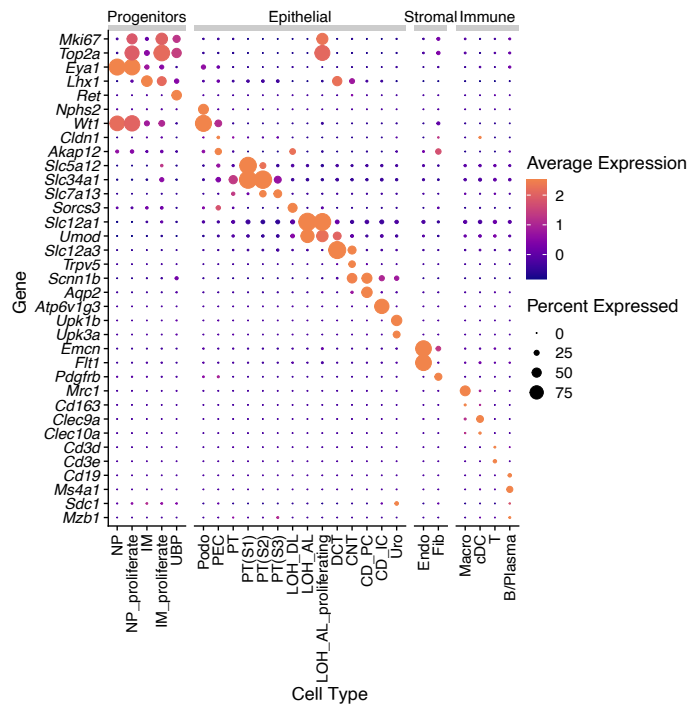
Extended data is available for this paper at <https://doi.org/10.1038/s41588-025-02161-x>.

Supplementary information The online version contains supplementary material available at <https://doi.org/10.1038/s41588-025-02161-x>.

Correspondence and requests for materials should be addressed to Li Ding or Feng Chen.

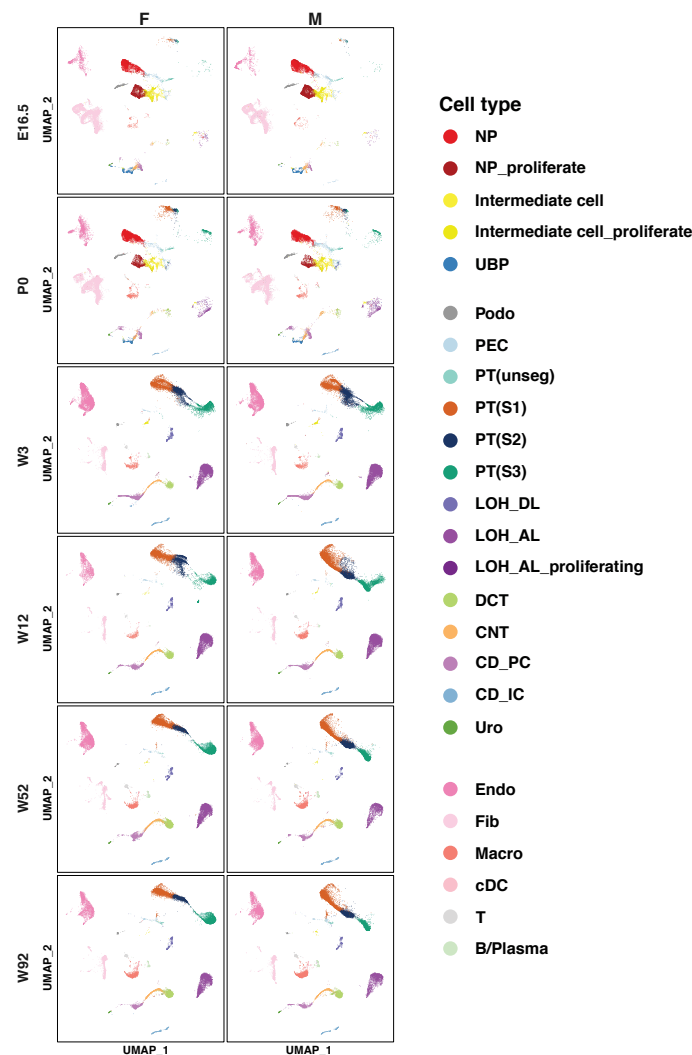
Peer review information *Nature Genetics* thanks the anonymous reviewer(s) for their contribution to the peer review of this work.

Reprints and permissions information is available at www.nature.com/reprints.



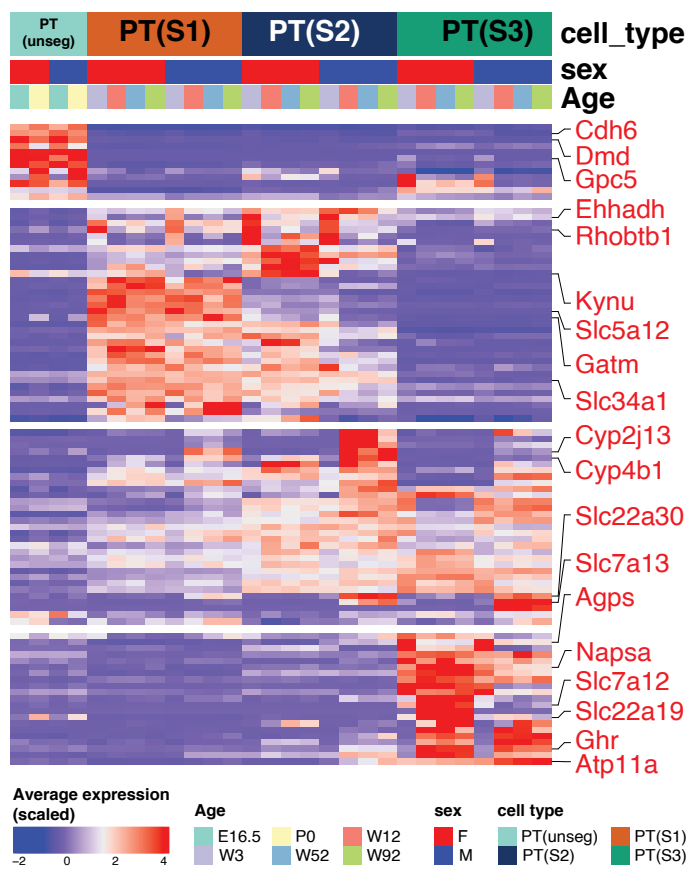
Extended Data Fig. 1 | Expression level and percentage for cell-type markers for multi-ome dataset. Dot size corresponds to the percentage of cells expressing a gene, and color indicates the average scaled expression in each cell type. NP, nephrogenic progenitor cell; IM, intermediate cell; UBP, ureteric bud progenitor cell; Podo, podocyte; PEC, parietal epithelial cells; PT, proximal tubules; PT(S1), proximal tubule segment 1; PT(S2), proximal tubule segment

2; PT(S3), proximal tubule segment 3; LOH_DL, loop of Henle descending limb; LOH_AL, loop of Henle ascending limb; DCT, distal convoluted tubule; CNT, connecting tubule; CD_PC, collecting duct principal cell; CD_IC, collecting duct intercalated cell; Uro, urothelium; Endo, endothelial cell; Fib, fibroblast; Macro, macrophage; cDC, conventional dendritic cell.


Extended Data Fig. 2 | UMAPs for cell distributions across ages and sexes.

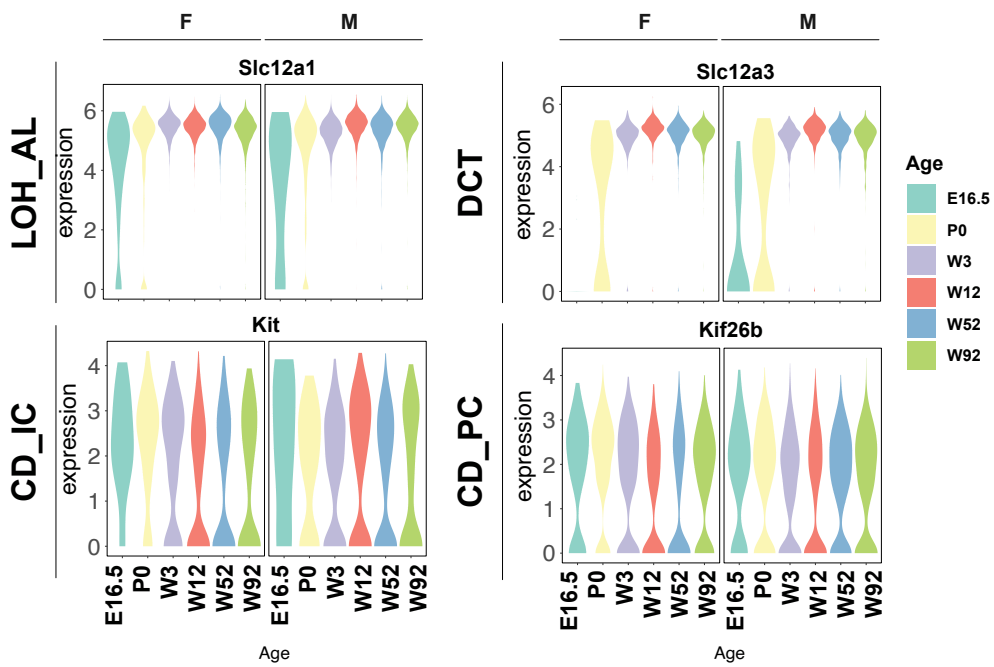
Cells are colored by cell type. NP, nephrogenic progenitor cell; UBP, ureteric bud progenitor cell; Podo, podocyte; PEC, parietal epithelial cells; PT, proximal tubules; PT(S1), proximal tubule segment 1; PT(S2), proximal tubule segment 2; PT(S3), proximal tubule segment 3; LOH_DL, loop of Henle descending limb; LOH_AL, loop of Henle ascending limb; DCT, distal convoluted tubule; CNT,

connecting tubule; CD_PC, collecting duct principal cell; CD_IC, collecting duct intercalated cell; Uro, urothelium; Endo, endothelial cell; Fib, fibroblast; Macro, macrophage; cDC, conventional dendritic cell; E16.5, embryonic 16.5; P0, newborn; W3, week 3; W12, week 12; W52, week 52; W92, week 92; F, female; M, male.



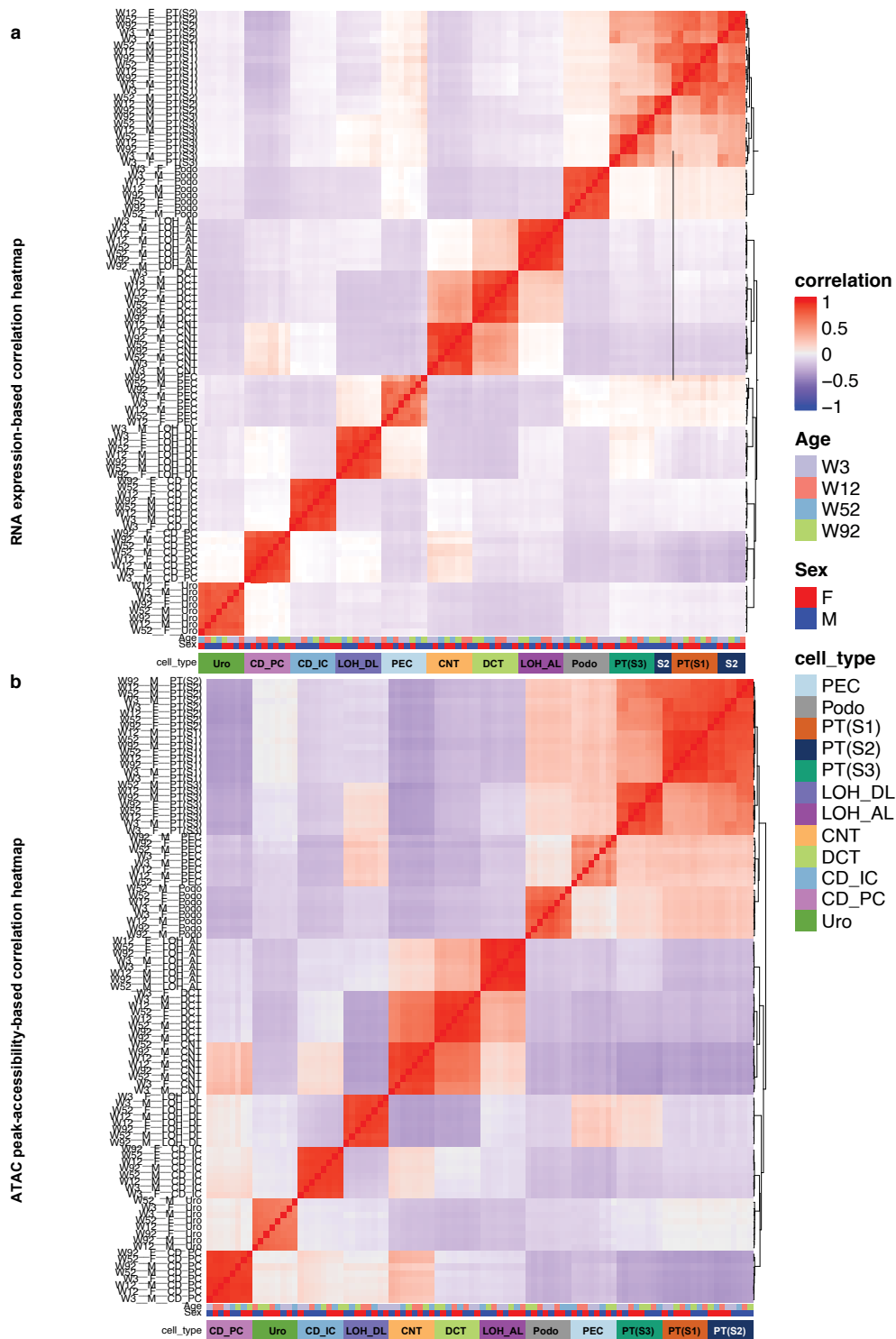
Extended Data Fig. 3 | Representative gene expression patterns in PT segments. A zoomed-in version of the heatmap from Fig. 2a focusing on PT segments. Genes of interest were highlighted in red. E16.5, embryonic 16.5;

P0, newborn; W3, week 3; W12, week 12; W52, week 52; W92, week 92; F, female; M, male; PT, proximal tubules; PT(S1), proximal tubule segment 1; PT(S2), proximal tubule segment 2; PT(S3), proximal tubule segment 3.



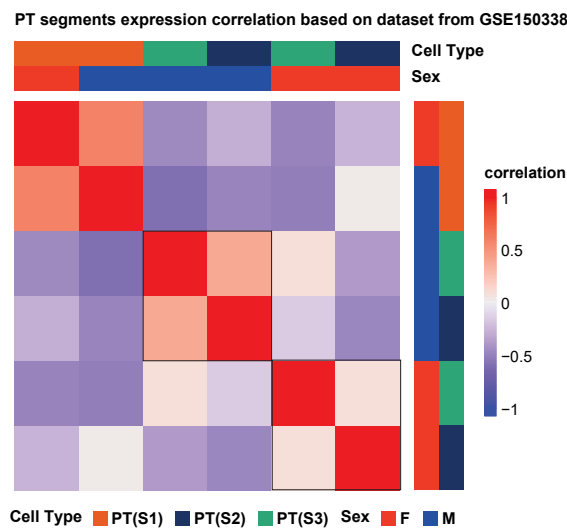
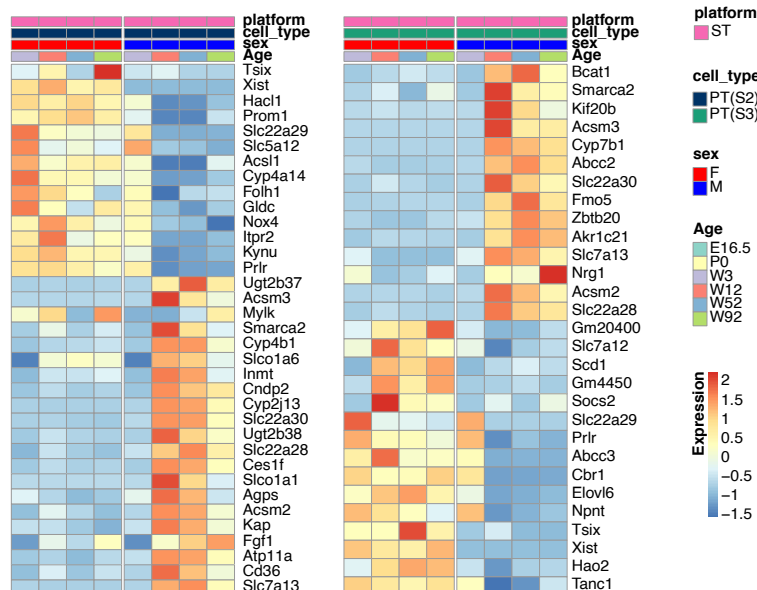
Extended Data Fig. 4 | Gene expression trend for LOH_AL, DCT, CD_IC and CD_PC cell-type marker genes. Violin plots showing cell-type marker genes with interesting expression trends across the lifespan for LOH_AL, DCT, CD_IC and CD_PC. Colors represent ages. E16.5, embryonic 16.5; P0, newborn; W3, week 3;

W12, week 12; W52, week 52; W92, week 92; F, female; M, male; LOH_DL, loop of Henle descending limb; LOH_AL, loop of Henle ascending limb; CD_PC, collecting duct principal cell; CD_IC, collecting duct intercalated cell.



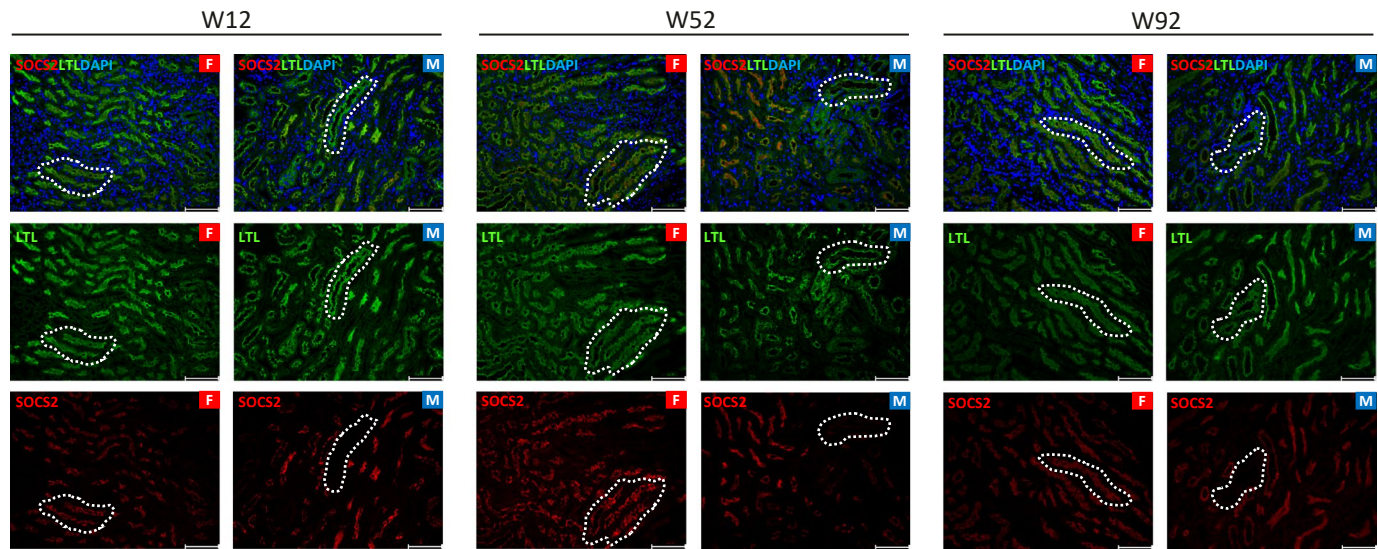
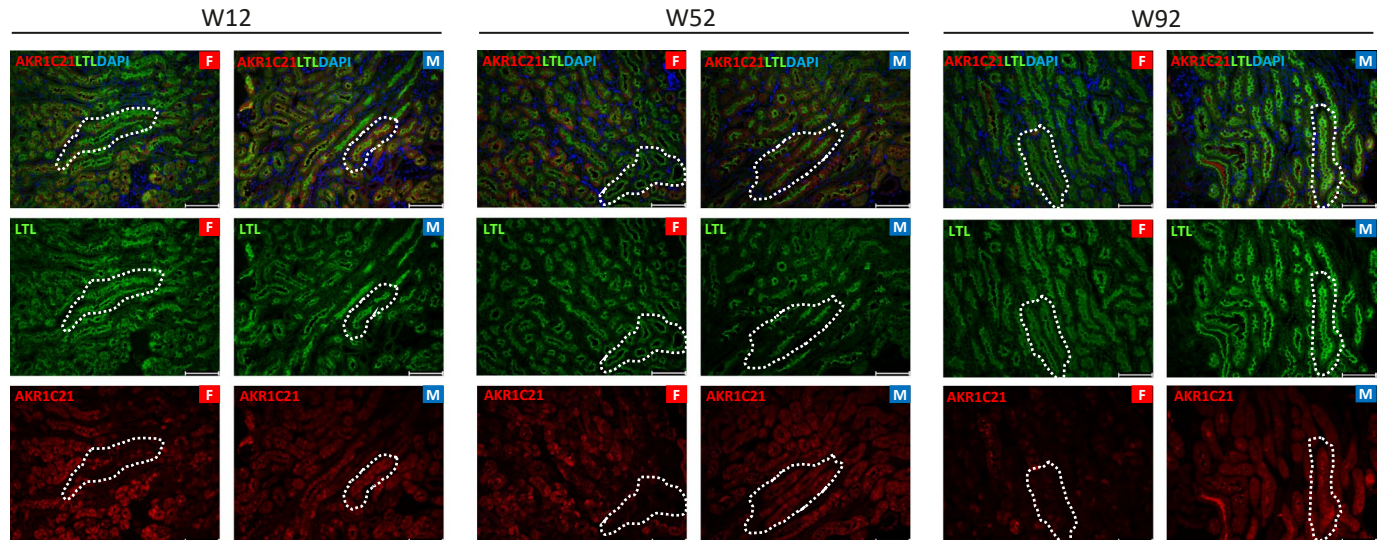
Extended Data Fig. 5 | Correlation among kidney cell types. **a**, Pearson correlation for gene expression among kidney cell types from W3, W12, W52 and W92 samples. **b**, Peak accessibility correlation among kidney cell types from W3, W12, W52 and W92 samples. E16.5, embryonic 16.5; PO, newborn; W3, week 3; W12, week 12; W52, week 52; W92, week 92; F, female; M, male; Podo, podocyte; PEC,

parietal epithelial cells; PT, proximal tubules; PT(S1), proximal tubule segment 1; PT(S2), proximal tubule segment 2; PT(S3), proximal tubule segment 3; LOH_DL, loop of Henle descending limb; LOH_AL, loop of Henle ascending limb; CD_PC, collecting duct principal cell; CD_IC, collecting duct intercalated cell.

a**b**

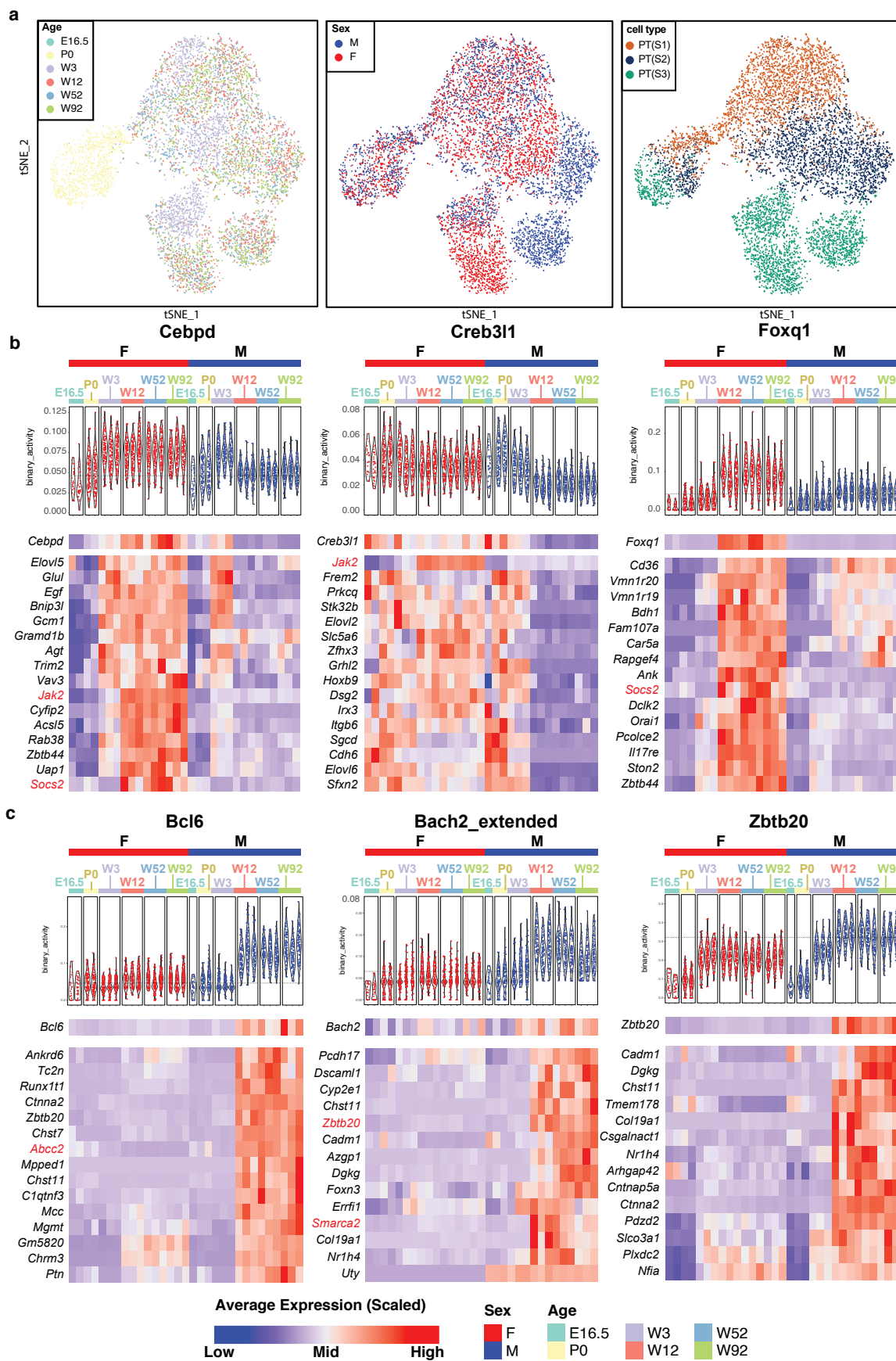
Extended Data Fig. 6 | Additional gene expression heatmaps. **a**, Heatmap showing the correlation of each PT segment (from each sex) expression between our dataset and the bulk RNA-seq dataset from [GSE150338](#). **b**, Heatmaps showing the Visium ST-based expression of top sex-biased DEGs of PT(S2) and PT(S3)

across different ages. E16.5, embryonic 16.5; P0, newborn; W3, week 3; W12, week 12; W52, week 52; W92, week 92; F, female; M, male; PT, proximal tubules; PT(S1), proximal tubule segment 1; PT(S2), proximal tubule segment 2; PT(S3), proximal tubule segment 3; ST, spatial transcriptomics.

a**b**

Extended Data Fig. 7 | SOCS2 and AKR1C21 protein expression comparison between sexes in mice. a,b, Immunofluorescence staining showing the protein expression pattern of (a) SOCS2 and (b) AKR1C21 in female and male mice ($n = 3$). Dashed curves indicate tubules that show the most obvious difference between

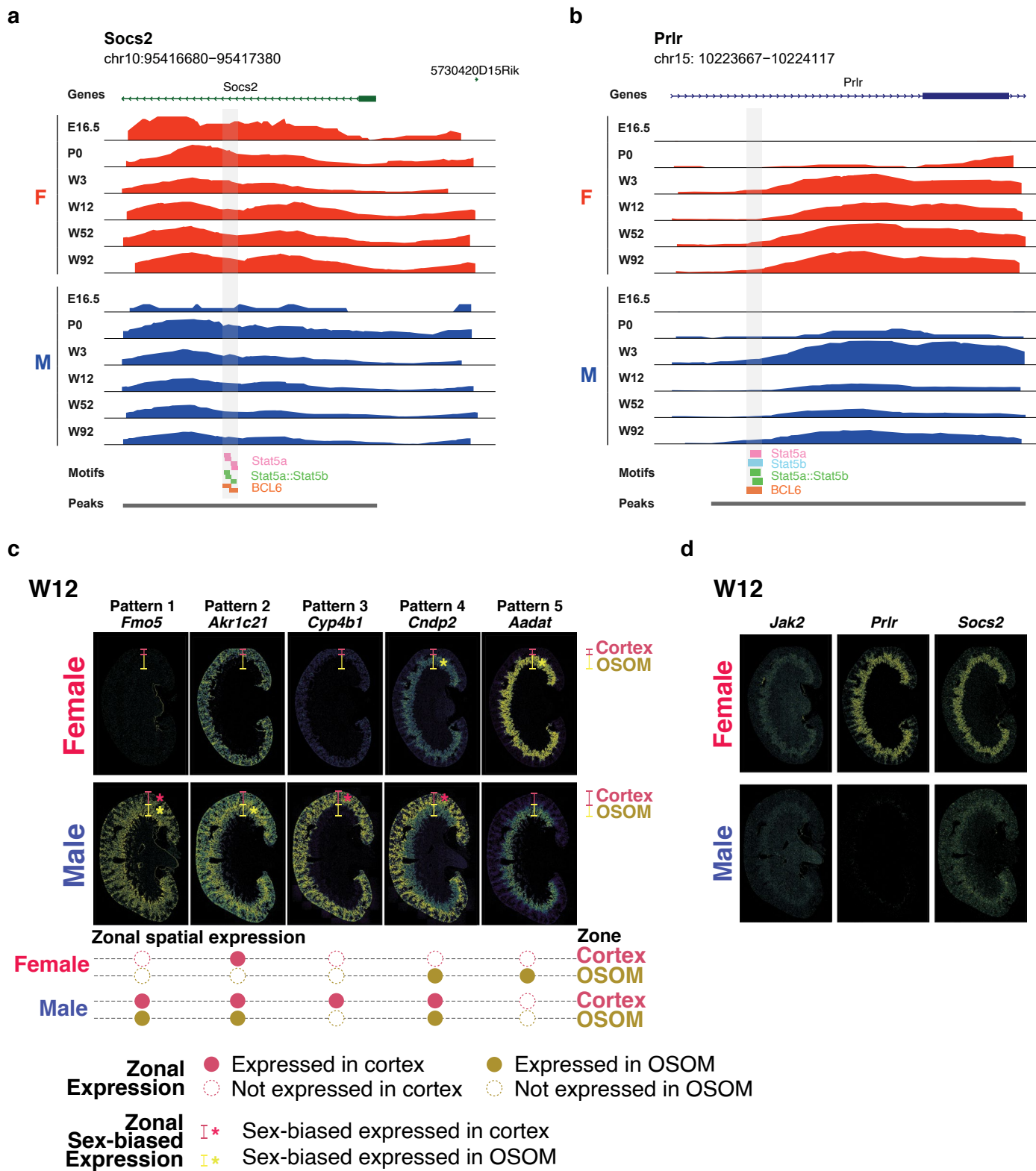
females and males. Scale bar, 100 μm . LTL (green) is used to label the PT segment. DAPI (blue) is used to label nuclei. Experiments are repeated >3 times with similar results. F, female; M, male; PT, proximal tubules; W12, week 12; W52, week 52; W92, week 92.



Extended Data Fig. 8 | See next page for caption.

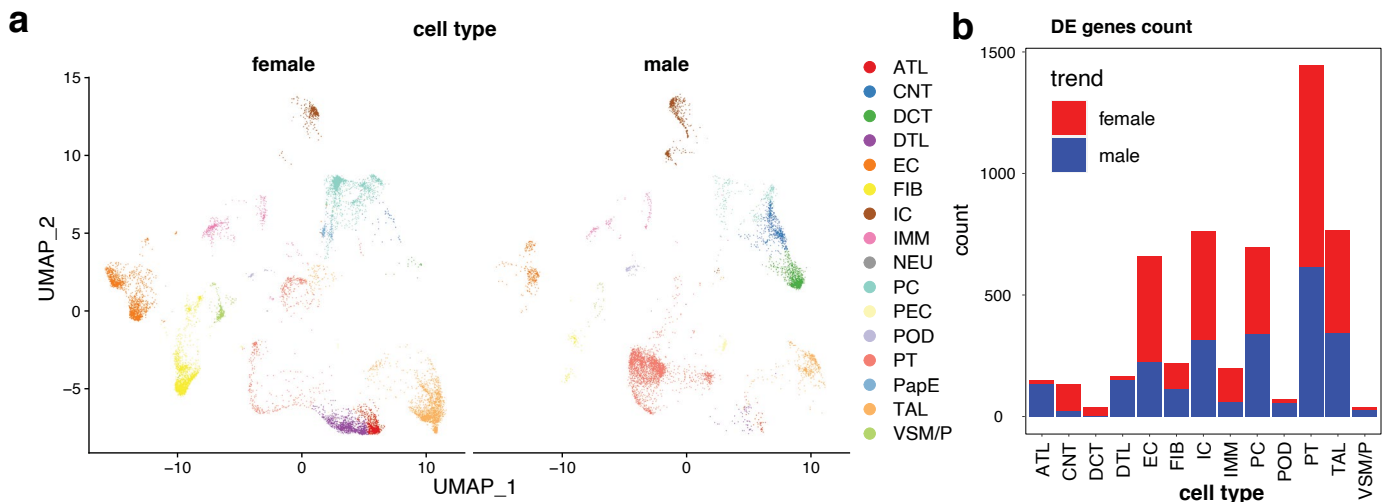
Extended Data Fig. 8 | tSNE plots and heatmaps from regulon analysis. **a**, tSNE plots based on SCENIC regulon AUC scores for each cell. From left to right, cells are colored by age, sex and cell type, respectively. **b**, Heatmaps showing the average expression of downstream targets of female-biased regulons, *Cebpd*,

Creb3l1 and *Foxq1*, for each sample. **c**, Heatmaps showing the average expression of downstream targets of male-biased regulons, *Bcl6*, *Bach2* and *Zbtb20*, for each sample. F, female; M, male; PT, proximal tubules; E16.5, embryonic 16.5; P0, newborn; W3, week 3; W12, week 12; W52, week 52; W92, week 92.



Extended Data Fig. 9 | Additional analysis for snATAC-seq and Xenium.
a,b, Peak accessibility for PT(S3) populations across ages and sexes. STAT5A, STAT5B and BCL6 within the promoter regions were highlighted. The peaks shown were the promoter regions of (a) Socs2 and (b) Prlr. **c**, Xenium single-cell spatial expressions of 5 sex-dimorphic spatial patterns in W12 mice. (Top) Zonal sex-biased spatial expression example annotated with range for Cortex

(red lines) and outer stripe of the outer medulla (OSOM; yellow lines). (Bottom) Diagram for the zonal pattern expression. Dots indicate the expression of the gene in that zone. **d**, Single-cell spatial expressions of Jak2, Prlr and Socs2 of W12 female and male mice using the Xenium platform. F, female; M, male; E16.5, embryonic 16.5; P0, newborn; W3, week 3; W12, week 12; W52, week 52; W92, week 92.


Extended Data Fig. 10 | UMAPs and DEG gene count for cell types in aging

kidneys. **a**, UMAPs highlighting the cell-type annotation for populations for each sex. **b**, Number of DEGs within each cell type between male and female. The color indicates female-biased (red) or male-biased (blue). ATL, loop of Henle thin ascending limb; CNT, connecting tubule; DCT, distal convoluted tubule;

DTL, loop of Henle thin descending limb; EC, endothelial cell; FIB, interstitial fibroblast; IC, collecting duct intercalated cell; IMM, leukocyte; NEU, neural cell; PC, collecting duct principal cell; PEC, parietal epithelial cell; POD, podocytes; PT, proximal tubule; PapE, papillary tips cell; TAL, loop of Henle thick ascending limb; VSM/P, renal interstitial pericyte; DEG, differentially expressed genes.

Reporting Summary

Nature Portfolio wishes to improve the reproducibility of the work that we publish. This form provides structure for consistency and transparency in reporting. For further information on Nature Portfolio policies, see our [Editorial Policies](#) and the [Editorial Policy Checklist](#).

Statistics

For all statistical analyses, confirm that the following items are present in the figure legend, table legend, main text, or Methods section.

n/a Confirmed

- The exact sample size (n) for each experimental group/condition, given as a discrete number and unit of measurement
- A statement on whether measurements were taken from distinct samples or whether the same sample was measured repeatedly
- The statistical test(s) used AND whether they are one- or two-sided
 - Only common tests should be described solely by name; describe more complex techniques in the Methods section.*
- A description of all covariates tested
- A description of any assumptions or corrections, such as tests of normality and adjustment for multiple comparisons
- A full description of the statistical parameters including central tendency (e.g. means) or other basic estimates (e.g. regression coefficient) AND variation (e.g. standard deviation) or associated estimates of uncertainty (e.g. confidence intervals)
- For null hypothesis testing, the test statistic (e.g. F , t , r) with confidence intervals, effect sizes, degrees of freedom and P value noted
 - Give P values as exact values whenever suitable.*
- For Bayesian analysis, information on the choice of priors and Markov chain Monte Carlo settings
- For hierarchical and complex designs, identification of the appropriate level for tests and full reporting of outcomes
- Estimates of effect sizes (e.g. Cohen's d , Pearson's r), indicating how they were calculated

Our web collection on [statistics for biologists](#) contains articles on many of the points above.

Software and code

Policy information about [availability of computer code](#)

Data collection No software was used for data collection

Data analysis Space Ranger(v1.3.0)
SoupX (v1.6.2)
SCENIC (v1.2.4)
Signac (v.1.5.0)
ChromVAR (v1.16.0)
JASPAR 2020 (v0.99.10)
clusterProfiler (v3.18.1)
RCTD (v2.0.0)
CytosPACE (v1.0.3)
Harmony (v0.1.0)
msigdbr (v7.5.1)
bcl2fastq (v2.20)
CellRanger-ARC (v2.0.0)
Xenium Explorer (v1.3.0)
scikit-image (v0.19.0)
Seurat (v.4.0.4, v4.1.1)

For manuscripts utilizing custom algorithms or software that are central to the research but not yet described in published literature, software must be made available to editors and reviewers. We strongly encourage code deposition in a community repository (e.g. GitHub). See the Nature Portfolio [guidelines for submitting code & software](#) for further information.

Data

Policy information about [availability of data](#)

All manuscripts must include a [data availability statement](#). This statement should provide the following information, where applicable:

- Accession codes, unique identifiers, or web links for publicly available datasets
- A description of any restrictions on data availability
- For clinical datasets or third party data, please ensure that the statement adheres to our [policy](#)

Raw data for multiome and Visium have been deposited into GEO: GSE252772. Raw and processed data for Xenium have been deposited into GEO: GSE286051.

Research involving human participants, their data, or biological material

Policy information about studies with [human participants or human data](#). See also policy information about [sex, gender \(identity/presentation\), and sexual orientation](#) and [race, ethnicity and racism](#).

Reporting on sex and gender

For samples from AMSBIO (<https://www.amsbio.com/>) and Origene (<https://www.origene.com/>), sex information were obtained from the vendor. For samples from Washington University, sex information were obtained from electronic health record system. For samples from Kidney Precision Medicine Project, sex information were obtained from: <https://cellxgene.cziscience.com/collections/bcb61471-2a44-4d00-a0af-ff085512674c>.

Reporting on race, ethnicity, or other socially relevant groupings

Race and/or ethnicity information is provided in the Supplementary Table 4.

Population characteristics

Population characteristics is provided in the Supplementary Table 4.

Recruitment

Normal adjacent tissue (NAT) samples were purchased from commercial vendors and selected from institutional collection with informed consent in concordance with Institutional Review Board (IRB) approval. There was no self-selection bias or other biases in the recruitment of patients.

Ethics oversight

Samples for IF were either purchased from AMSBIO (<https://www.amsbio.com/>) and Origene (<https://www.origene.com/>), or were collected with informed consent in concordance with Institutional Review Board (IRB) approval at the School of Medicine at Washington University in St Louis. IRB protocol is 201411135. Samples for snRNA-Seq analysis were download from online resource (<https://cellxgene.cziscience.com/collections/bcb61471-2a44-4d00-a0af-ff085512674c>).

Note that full information on the approval of the study protocol must also be provided in the manuscript.

Field-specific reporting

Please select the one below that is the best fit for your research. If you are not sure, read the appropriate sections before making your selection.

Life sciences Behavioural & social sciences Ecological, evolutionary & environmental sciences

For a reference copy of the document with all sections, see nature.com/documents/nr-reporting-summary-flat.pdf

Life sciences study design

All studies must disclose on these points even when the disclosure is negative.

Sample size

Sample sizes were chosen based on the availability of samples. No specific statistical methods were used to predetermine sample size. We make sure all statistical measurements are based on at least N=3 for the mouse study. IF was done on 3 independent repeats for both mice tissues and human tissues. There are only 2 male NAT samples available from KPMP so N=2 was used for human snRNA-Seq related analysis. For samples used for demonstration purpose (Xenium ST and Phenocycler), N=1 for Phenocycler, N=2 for Xenium are used.

Data exclusions

No data were excluded for the mouse study. For snRNA data from Kidney Precision Medicine Project, to reduce confounding factors in sex difference analysis as much as possible, we selected patient samples without acute kidney injuries or chronic kidney diseases, whose ages are under 60, and whose ethnicity are Caucasian.

Replication

For mouse multiome data analysis, at least 3 biological replicates were used given each age and sex. IF experiment findings were verified by using 3 independent samples. CODEX experiment findings were verified by using 8 random imaging areas. All attempts at replication were successful. Each experiment was repeated independently for at least 3 times with similar results.

Randomization

The mice were either randomly sent from Jackson Lab or randomly inbred in-house, then randomly allocated into experimental groups. The Investigators were not blinded to allocation during experiments and outcome assessment.

Blinding

Blinding was not relevant to our study because we aimed at comparing between female and male kidneys, so when samples were collected, we make sure the right sex was collected.

Reporting for specific materials, systems and methods

We require information from authors about some types of materials, experimental systems and methods used in many studies. Here, indicate whether each material, system or method listed is relevant to your study. If you are not sure if a list item applies to your research, read the appropriate section before selecting a response.

Materials & experimental systems

- | | |
|-------------------------------------|---|
| n/a | Involved in the study |
| <input type="checkbox"/> | <input checked="" type="checkbox"/> Antibodies |
| <input checked="" type="checkbox"/> | <input type="checkbox"/> Eukaryotic cell lines |
| <input checked="" type="checkbox"/> | <input type="checkbox"/> Palaeontology and archaeology |
| <input type="checkbox"/> | <input checked="" type="checkbox"/> Animals and other organisms |
| <input checked="" type="checkbox"/> | <input type="checkbox"/> Clinical data |
| <input checked="" type="checkbox"/> | <input type="checkbox"/> Dual use research of concern |
| <input checked="" type="checkbox"/> | <input type="checkbox"/> Plants |

Methods

- | | |
|-------------------------------------|---|
| n/a | Involved in the study |
| <input type="checkbox"/> | <input checked="" type="checkbox"/> ChIP-seq |
| <input checked="" type="checkbox"/> | <input type="checkbox"/> Flow cytometry |
| <input checked="" type="checkbox"/> | <input type="checkbox"/> MRI-based neuroimaging |

Antibodies

Antibodies used

SOCS2 (#34-6900, Invitrogen, 1:50), AKR1C1 (Orthologous to mouse AKR1C21) (#LS-B15860-200, LSBio, 1:100), INMT (#PA5-97875, Invitrogen, 1:100), SCD (Orthologous to mouse SCD1) (#MA1-26155, Invitrogen, 1:50), CYP4B1 (#PA5-106560, Invitrogen, 1:100), Alexa Fluor™ Plus 594 (#32754, Invitrogen, 1:1000), Alexa Fluor™ Plus 647 (#32795, Invitrogen, 1:1000), Alexa Fluor™ Plus 647 (#32787, Invitrogen, 1:1000), Alexa Fluor™ 488 (#21206, Invitrogen, 1:1000), LTL (#FL1321, Vector Labs, 1:300), SMA (#MA1-06110, eBiosciences, 1:100), AQP1 (#ab178352, Abcam, 1:100), LRP (#ab76969, Abcam, 1:100), CALB1 (#ab233018, Abcam, 1:200), UMOD (#ab223540, Abcam, 1:100), AQP2 (#ab230170, Abcam, 1:200), CK19 (#ab195872, Abcam, 1:200), CD31 (#4450017, Akoya, 1:100), Collagen IV (#4550122, Akoya, 1:100), E-cadherin (#4250021, Akoya, 1:400), PanCytokeratin (#4450020, Akoya, 1:200), Podoplanin (#4250004, Akoya, 1:400), Vimentin (#4450050, Akoya, 1:100), Ki67 (#4250019, Akoya, 1:800), CD3e (#4550119, Akoya, 1:100), CD4 (#4550112, Akoya, 1:100), CD8 (#4250012, Akoya, 1:800), CD68 (#4550113, Akoya, 1:200).

Validation

SOCS2 (#34-6900, Invitrogen) was validated by IHC in PMID: 19470084 in C57BL/6N mice liver. AKR1C1 (#LS-B15860-200, LSBio) was validated by IHC in human adrenal by the manufacturer at 1:100 with LSbio standardized validation process provided on the manufacturer's website. INMT (#PA5-97875, Invitrogen) was validated by IHC in human lung cancer tissues by the manufacturer at 1:100. SCD (#MA1-26155, Invitrogen) was validated by knockdown to ensure the antibody binds to the antigen stated by the manufacturer. CYP4B1 (#PA5-106560, Invitrogen) was validated by WB in COLO cells by the manufacturer. AQP1 (#ab178352, Abcam) was confirmed in IHC with multi-tissue microarray (TMA) validation as stated on the manufacturer's website. LRP (#ab76969, Abcam) was confirmed with 52 publications as stated on the manufacturer's website. CALB1 (#ab233018, Abcam), UMOD (#ab223540, Abcam), AQP2 (#ab230170, Abcam), and CK19 (#ab195872, Abcam) was validated through Abcam's "Advanced Validation" process as stated on the manufacturer's website. CD31 (#4450017, Akoya), Collagen IV (#4550122, Akoya), E-cadherin (#4250021, Akoya), PanCytokeratin (#4450020, Akoya), Podoplanin (#4250004, Akoya), Vimentin (#4450050, Akoya), Ki67 (#4250019, Akoya), CD3e (#4550119, Akoya), CD4 (#4550112, Akoya), CD8 (#4250012, Akoya) and CD68 (#4550113, Akoya) were meticulously designed, pre-conjugated, validated, and manufactured by Akoya as stated on the manufacturer's website.

Animals and other research organisms

Policy information about [studies involving animals](#); [ARRIVE guidelines](#) recommended for reporting animal research, and [Sex and Gender in Research](#)

Laboratory animals

We used week-3, week-12, week-52, week-92 C57BL/6J mice (Strain #:000664) which purchased from the Jackson Laboratory; we inbred C57BL/6J mice (Strain #:000664) which purchased from the Jackson Laboratory to get E16.5 and P0 mice in house with temperature range from 68-79°F (20-26°C), humidity: 30-70%, and a diurnal cycle light (dark cycle of 12 hours on and 12 hours off).

Wild animals

No wild animals were used.

Reporting on sex

Findings apply to both sexes. Sex was considered in study design. Female and male mice older than or equal to 3 weeks were directly purchased from Jackson Lab. Mice younger than 3 weeks were inbred in house and sexes were determined using qPCR. In summary, we used mice that were at embryos (E16.5), newborns (P0), 3 weeks (W3), 12 weeks (W12), 52 weeks (W52), and 92 weeks (W92). 12 mice were collected for both E16.5 and P0, while 6 mice were collected for each remaining time point. For each time point, male and female mice were equally represented.

Field-collected samples

Field-collected samples were not involved in our study.

Ethics oversight

All animal experiments were approved by the Institutional Animal Care and Use Committee (IACUC) office (protocol #22-0233) in Washington University in Saint Louis.

Note that full information on the approval of the study protocol must also be provided in the manuscript.

Plants

Seed stocks	None
Novel plant genotypes	NA
Authentication	NA